Investigation of the effects of platelet morphology and flow conditions on the elastic behavior of discontinuous fiber composites

James Davey

A thesis
submitted in partial fulfillment of the
requirements for the degree of

Master of Science

University of Washington

2022

Committee:

Marco Salviato

Jinkyu Yang

Program Authorized to Offer Degree:

William E. Boeing Department of Aeronautics and Astronautics

University of Washington

Abstract

Investigation of the effects of platelet morphology and flow conditions on the elastic behavior of discontinuous fiber composites

James Davey

Chair of the Supervisory Committee:
Marco Salviato
William E. Boeing Department of Aeronautics and Astronautics

In this work, the effects of platelet morphology and manufacturing flow conditions on the elastic behavior of discontinuous fiber composites are investigated. Two different platelet morphologies are explored: a narrow platelet and a square platelet with identical fiber lengths are used to manufacture specimens using two different processes to produce a quasi-isotropic low-flow condition, and a partially aligned high-flow condition. Three different specimen thicknesses are explored. Investigation of the elastic properties are carried out by means of tensile tests on unnotched specimens. This information is used to conduct a virtual study of the fiber orientation space by simulation with explicit modelling of the mesostructure and use of finite element analysis to determine the elastic properties.

From the tensile testing it is observed that the thickness has negligible or slight impact on the longitudinal elastic moduli. However, the flow condition has a significant effect on the longitudinal elastic modulus, with low-flow specimens falling 9.2% to 22.5% below a quasi-isotropic reference, and high-flow specimens outperforming the quasi-isotropic reference from 0.8% to 3.7%. Platelet morphology is similarly tied to elastic modulus, with square platelet specimens consistently underperforming from 2.9% to 14.8% compared to narrow platelet specimens.

An exploration of fiber orientation state is undertaken using microcomputed tomography. It is shown that flow condition has a significant effect on the orientation states in-plane and out-of-plane, with high-flow processes inducing significant longitudinal alignment.

Simulations were undertaken which showed agreement within 2% for the elastic modulus seen in the experimental results, but significantly, with scatter much lower than that observed experimentally.

TABLE OF CONTENTS

LIST OF FIGURES

LIST OF TABLES

NOMENCLATURE

ψ: Probability density function for fiber orientation distributions

ϕ: Out-of-plane fiber orientation

θ: In-plane fiber orientation

a_{ij}: Component ij of a 2nd-order orientation tensor

B_U: Upper boundary condition on a uniform probability distribution

B_L: Lower boundary condition on a uniform probability distribution

E_{11}: Longitudinal elastic modulus

E_{22}: Transverse elastic modulus

$\bar{p}$: Unit orientation vector

p_i: Component i of a unit orientation vector

w: Narrow platelet width

ACRONYMS

CMO: Boeing's Commercial Market Outlook

COV: Coefficient of Variation

CFC: Continuous Fiber Composite

CLT: Classical Laminate Theory

DFC: Discontinuous Fiber Composite

DIC: Digital Image Correlation

FEM: Finite Element Method

HF: High-Flow

LF: Low-Flow

NP: Narrow Platelet

NP-LF: Narrow Platelet Low-Flow specimens

NP-HF: Narrow Platelet High-Flow specimens

PDF: Probability density function

PEKK: Poly-Ether-Ketone-Ketone

QI: Quasi-Isotropic

RVE: Representative Volume Element

RLVE: Representative Laminate Volume Element

ROS: Randomly-Oriented Strand

SP: Square Platelet

SP-LF: Square Platelet Low-Flow specimens

SP-HF: Square Platelet High-Flow specimens

UNT: UnNotched Tension

GLOSSARY

CARBON FIBER TOW: A ribbon of typically thousands of unidirectional carbon fiber strands preimpregnated with a resin matrix

COMPOSITE: A material system comprised of two (or more) phases: a reinforcement and a matrix at a minimum

COEFFICIENT OF VARIATION: The ratio of the standard deviation to the mean of a given distribution

DIGITAL IMAGE CORRELATION: Optical method to measure the deformation over the surface of a specimen using image registration and tracking

ELASTIC MODULUS: A measurement of a material's resistance to elastic deformation when stressed

FINITE ELEMENT ANALYSIS: A numerical method for solving partial differential equations by subdividing a complex structure into small, simple parts called "finite elements"

LAMINAE: A lamina, or ply, is a layer of carbon fiber embedded in a matrix

LAMINATE: A laminate is a structure composed of two or more lamina

PLATELET: Small discrete chips cut from carbon fiber tows

PREPREG: Carbon fiber tows ready-made for manufacturing

THERMOPLASTIC: A composite matrix polymer which is fully polymerized; solid at room temperature and malleable when heated

THERMOSET: A composite matrix polymer which undergoes polymerization when heated, permanently curing

WAVINESS: A type of out-of-plane behavior where a platelet deforms during manufacturing in a manner resembling a wave

ACKNOWLEDGMENTS

There are many people for whom I wish to express gratitude for their roles in contributing to my successes in my time at the University of Washington.

Firstly, to my advisor Professor Marco Salviato, I thank you for your mentorship, and for the extensive guidance and feedback you have given me throughout the course of this work, and in the research studies I have been involved in throughout my undergraduate education. Your encouragement of my questions and validation of my efforts means a lot to me.

Likewise, to Professor Jinkyu Yang, thank you for serving on my committee, and more foundationally for getting me involved in research into discontinuous fiber composites as a Junior in the first place. I am grateful to have been afforded the opportunity to remain engaged in this research ever since. To you and Marco both, thank you for supporting me in my application to graduate school and supporting me in this work.

I would also like to recognize and thank Seunghyun Ko, who took a leading role in guiding the several research efforts I have been involved with over the last four years. The opportunity to work on discontinuous fiber composites and learn more about these materials has been valuable to me. Seung, I also want to thank you for your offhand question asking if I had considered pursuing a master's degree; I had not, and without that question I doubt I would have. Your encouragement has made this all possible.

I would also like to thank Troy Nakagawa and Zhisong Chen for their contribution of microcomputed tomography and micrography which I used in the analysis portions of this work.

Lastly, I also wish to express appreciation and gratitude to my girlfriend, to my fam-

ily, and to my friends for their continued support throughout my education and especially my time as a graduate student. Your support throughout this long and sometimes deeply emotional journey has made it all worth it, and without you it would not have been possible.

DEDICATION

To Tiffany

Chapter 1
INTRODUCTION

The 2019 coronavirus pandemic has been devastating to the aviation industry. More than 40 commercial airlines have ceased or suspended operations, and it was reported that by June 2020, airlines on average had only eight and a half months of cash remaining to finance operations [1]. Further, passenger traffic collapsed to levels not seen since 1999, erasing 21 years of steady growth in the air travel industry at the worst of the crisis, gradually recovering to approximately 60% of 2019 levels by August 2020, where it has held steady [1]. The International Air Transport Association does not expect a full recovery of passenger traffic to 2019 levels until 2024 under even their most optimistic outlooks [1]. These changes have had dramatic impacts on airline revenue. In 2019, revenue was $838 billion, and this has fallen to $372 billion in 2020 [2]. After labor costs, fuel is an airline's largest operational expense [3, 4], accounting for between 20-30% of total expenditures [5]. In 2019, commercial airlines consumed 95 billion gallons of fuel globally, but due to the ongoing coronavirus pandemic, 2020 saw consumption fall to 52 billion gallons [6]. With the financial squeeze brought on by the dramatic curtailment of air travel due to the coronavirus pandemic, incentives to reduce costs and economize are greater than ever before.

As airlines the world over adapt to the changing environments brought on by the coronavirus pandemic, the long-term trajectory remains favorable. Boeing's Commercial Market Outlook (CMO) from 2019, prior to the coronavirus pandemic, forecast 44,040 aircraft deliveries, 19,000 of which would be to replace aging aircraft [7]. The 2020 CMO, accounting

for the coronavirus pandemic, has revised this figure, marginally, to 43,110 deliveries, 20,700 of which are expected to be replacements [8] as airlines the world over move up retirement timetables to make way for more economical aircraft as cost saving measures [3]. The production and delivery of newer and more advanced aircraft will continue in spite of the coronavirus pandemic, and will increasingly incorporate advanced carbon composites in their construction to respond to the increasing demands for lighter, more fuel-efficient aircraft.

1.1 A Composites Overview

1.1.1 What is a composite?

A composite is a material system, composed of two-or-more phases at the macroscopic scale. The purpose of this system is to provide for a material that is stronger than the sum of its parts, with each phase compensating for the weaknesses of the other. Typical formulations are a stronger phase, the reinforcement, such as glass or carbon fibers, embedded in a weaker phase, the matrix, such as an epoxy resin or ceramic. The strength, durability, fracture toughness and other key properties important to aerospace and other industries are strongly governed by a number of key parameters, chief among them the fiber-volume fraction: the ratio of reinforcing fiber to matrix by volume, and the distribution and orientation of the reinforcing fibers. A homogeneous or uniform composite material has a distribution and alignment that is the same from region to region within a structure made from that material. A heterogeneous composite material by contrast has a spatially varying distribution of orientations and densities of the reinforcing fiber [9].

1.1.2 Advantages and limitations

Advantages of a composite are many. At the micromechanics scale, composites feature high stiffness and strength, with the low fracture toughness and damage tolerance of the reinforcing fibers compensated for by a ductile matrix that facilitates dispersion of energy

throughout the entire material system. The power of composites arises from the flexibility of the material system to be tailored to a specific application by exploiting the anisotropic characteristics. Strength along loading directions can be specifically targeted and improved by sacrificing strength along directions that are not subject to significant loads, with less material than with traditional isotropic metals. A composite material system, however, has a number of limitations that must be considered when designing structures that use it. Heterogeneities in the microstructure lead to high scatter in material properties, and localized stress concentrations develop around the reinforcing fibers themselves at the fiber-matrix interfaces, which reduces the strength at these locations and may lead to failure under loads that are lower than expected. Additionally, manufacturing structures with a composite material often involves substantial opportunity for the introduction of foreign objects and air, leading to inclusions, blisters, and voids that weaken the structure overall, and resin will often pool in areas within the structure where the arrangements of the reinforcing fiber leaves gaps, as shown in figure 1.1. These weak spots may lead to premature failure of a structure and can be difficult to detect and repair [9].

1.1.3 Classifications

Composites may be broken down into three main categories: particulate, continuous, and discontinuous. A particulate composite has a reinforcing phase comprised of small particles of glass, nylon, carbon fiber, and other materials intermixed with a matrix to form a quasi-homogeneous, quasi-isotropic material [9]. A continuous composite has unidirectional or woven, long and continuous fibers embedded in a matrix, as shown in figures 1.2a and 1.2b [9]. These composites are the most common type used in industry [9], and notably the Boeing 787's fuselage is fabricated from continuous carbon fiber tows laid down by large automated mandrels [11], seen in figure 1.3. A discontinuous composite uses chopped, short fibers, which are long relative to their diameter, embedded in a matrix [9]. These fibers may

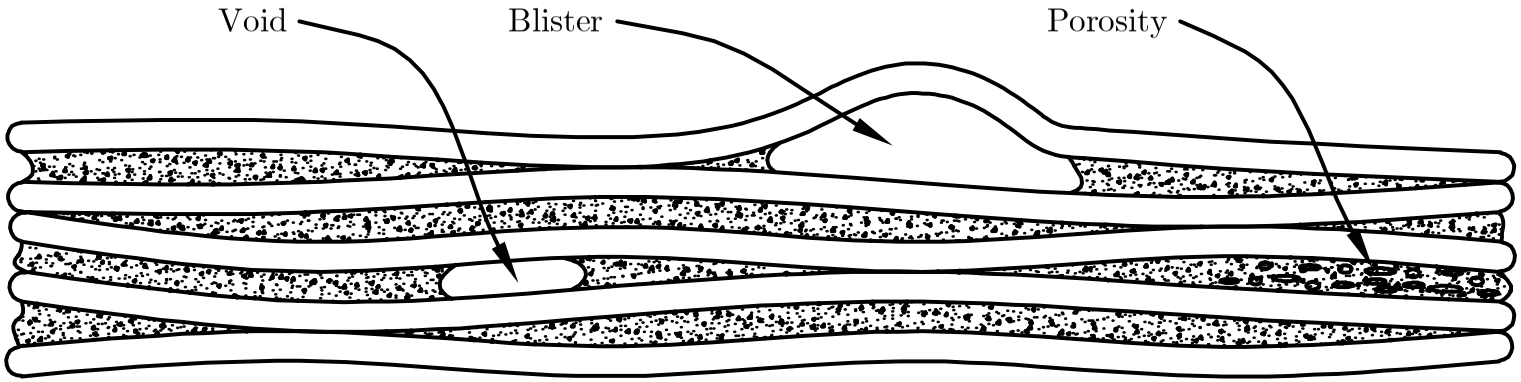

(a) Manufacturing defects

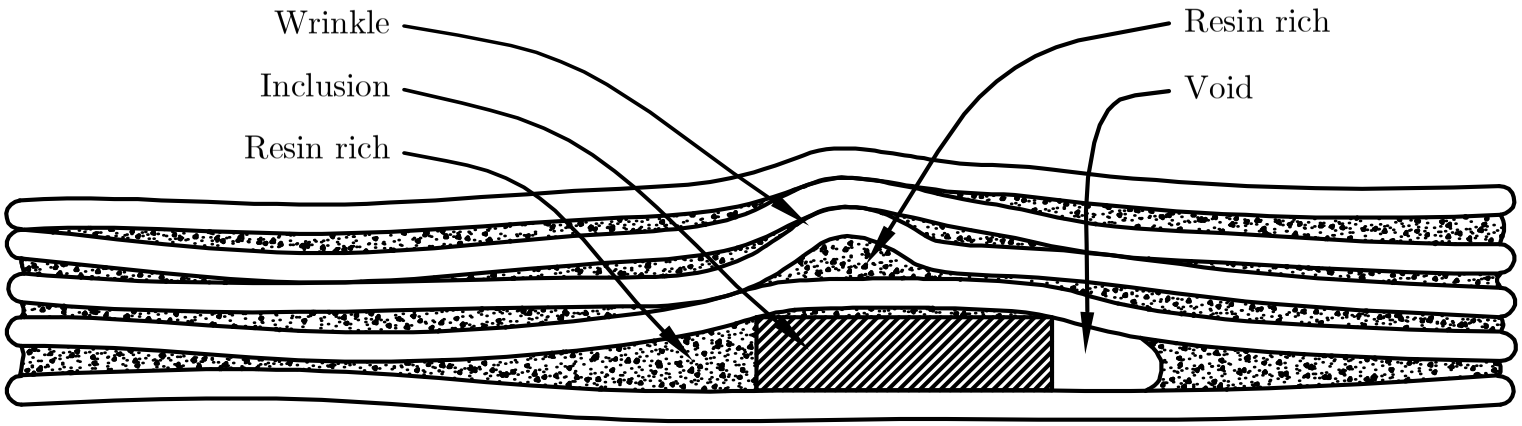

(b) Foreign object inclusions

Figure 1.1: Manufacturing defects and foreign object inclusions in fiber-reinforced composite systems

Figures reproduced from Unndorsonn et. al. with permission [10]

be aligned or randomly oriented as shown in figures 1.2c and 1.2d.

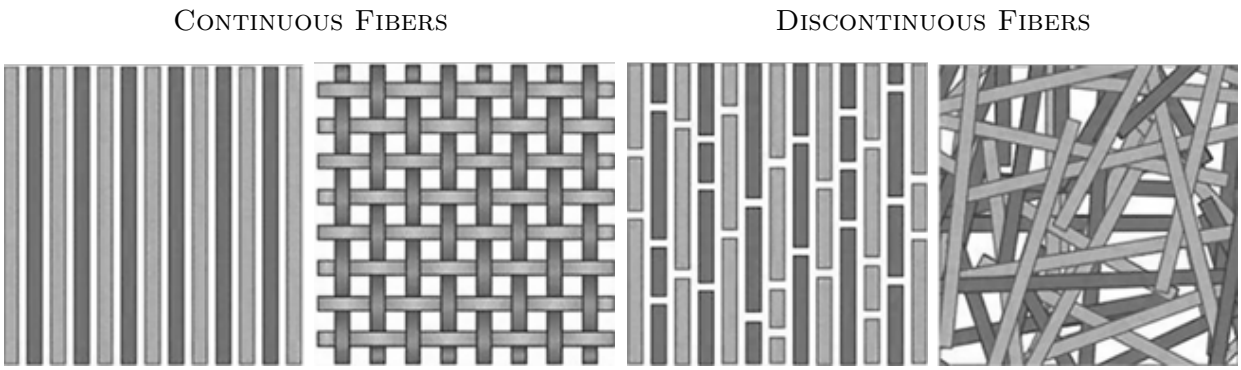

Figure 1.2: Visualization of the assorted classes of composite fiber arrangements
Images copyright LibreTexts [12]

1.1.4 Types of matrices

There are four major types of matrices: polymeric, metallic, ceramic, and carbon, each with unique advantages and disadvantages and specific use cases. Polymeric matrices are the most extensively used in industry, coming in two main flavors, thermoset and thermoplastic [9, 14].

Thermoset polymers (thermosets) are most commonly used for their flexibility with manufacturing, allowing work at room temperature and easy application due to their uncured, liquid state. Curing locks the molecular bonds through a catalytic chemical reaction[14], undergoing polymerization and cross-linking when heated and held above the cure temperature [9]. Thermosets have good mechanical properties and are cheap and easy to work with, however there is increased temperature sensitivity relative to other polymers [9].

(a) Automatic Fiber Placement **(b)** Aircraft-sized autoclave

Figure 1.3: Layup and curing of a Boeing 787 forward section by Spirit AeroSystems
Images copyright Daniel Terdiman [13]

Thermoplastic polymers (thermoplastics) by contrast are fully polymerized, solid at room temperature and malleable when heated to high temperatures and pressures [9, 14]. These features allow thermoplastics to be used with heated compression molding, hot forming, and injection molding manufacturing techniques, allowing for a more complex range of shapes and structural features than are possible with thermosets [9].

1.1.5 Damage mechanisms and failure modes

A composite material is complex, and in most situations failure does not occur due to a single factor but rather the progressive accumulation of a variety of damage types. Surface defects introduced during the manufacture of carbon fibers [10] create weakness from which cracks may initiate, fracturing the fiber [15], as shown in figure 1.4. Debonding occurs at the interface of the fiber and matrix, preventing the matrix from distributing stresses to the fiber, which reduces the strength and stiffness at that location, leading to failure under load [10]. Delamination and matrix cracking are a result of tensile stresses where fiber plies cross, due to a mismatch in the Poisson's ratio [15]. One fiber may be aligned favorably

with the load, while another is orthogonal to the loading direction. The matrix interface transferring the load between these two fibers experiences stress as the two fibers deform differently, leading the cracks. The accumulation of all these types of damage reduces the effective elastic modulus of a composite part, and ultimately leads to crack initiation and fracture.

1.2 Carbon Composites in Industry

Advances in carbon composite utilization have enabled much of the improvement in fuel efficiency and cost reductions in modern aircraft. For example, the Boeing 787 is among the most advanced composite commercial aircraft yet designed, being 50% composites by weight, consuming 20% less fuel, and reducing maintenance and operating costs by 30% and 15% respectively [11] compared to the family of aircraft it replaces. The Boeing 787 aircraft itself weighs 20% less than a comparable aluminum aircraft such as the Boeing 767 [16]. The fuselage of the Boeing 787 is a single monocoque construct, eliminating skin splices [11], using 50,000 fewer fasteners, and allowing greater internal pressure than conventional aircraft [17]. In addition to the greater internal pressure afforded by the stronger, lighter monocoque shell, the window frames in the Boeing 787 are similarly constructed from compression molded composite platelets, which allows them to be larger and 50% lighter than conventional window frames [18]. In the Boeing 777, the composite tail requires 35% fewer scheduled maintenance hours than the Boeing 767's aluminum tail, despite being 25% larger [16]. These improvements arise from the unique opportunities that carbon composites afford on account of their material properties and anisotropy.

Advantages offered by carbon composites are numerous and significant. From a materials standpoint, the favorable strength-to-weight ratio as compared with industry standard metals such as aluminum and titanium are a major point of interest, with carbon composites typically being one-half and one-third as dense respectively, while offering greater strength

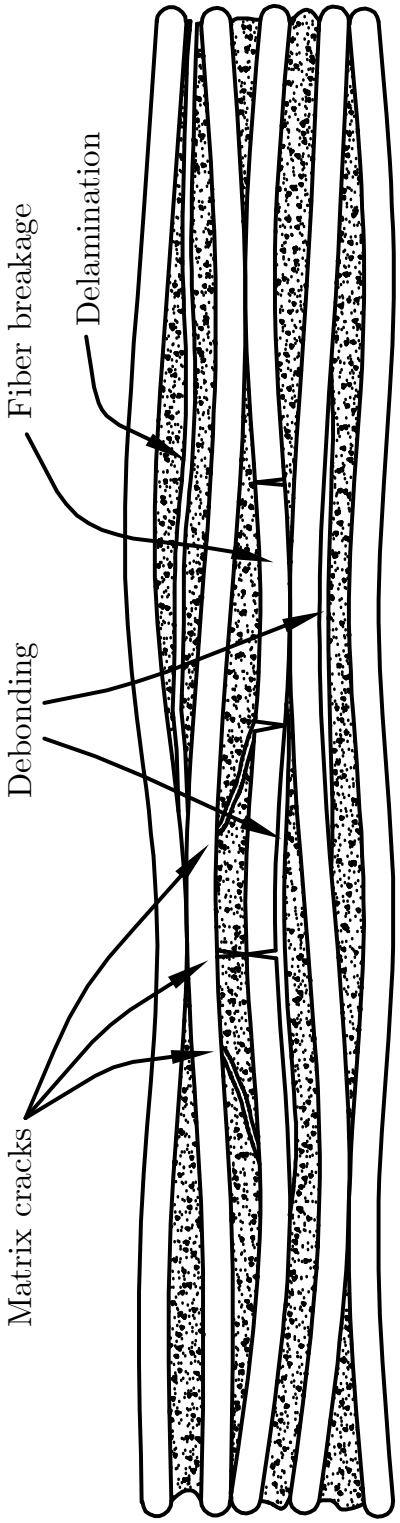

Figure 1.4: Damage mechanisms in fiber-reinforced composite systems

Figures reproduced from Unndorsonn et. al. with permission [10]

and stiffness; see table 1.1. Further, composites may be tailored with custom fiber layups to the loading conditions of a given component due to their anisotropy in a way not possible with isotropic metallics. As tow-based continuous carbon composite structures continue to be integrated into structural elements such as the skin, stringers and frames that comprise the fuselage, there is a need to address the challenges of interfacing composite elements with metal connectors and fasteners [19], which experience galvanic corrosion at the metal-composite interfaces. While carbon composites do not experience the corrosion and thermal stability issues of conventional metal parts [20], the current aerospace processes for manufacture of composite parts are difficult and expensive for the more complex geometries needed for the connector elements [19]. Discontinuous fiber composites provide a promising solution to this problem.

Table 1.1: Material properties of common aerospace-grade composites and metals

Material	Density (g/cc)	T Modulus (GPa)	T Strength (MPa)	CTE (μm/m-°C)	Elongation (%)
Titanium[a]	4.43	114	1100	8.60	10
Aluminum[b]	2.7	68.9	276	23.6	17
T700[c]	1.517	125	2171	-0.3	2
T800[d]	1.540	148	3006	-0.4	2

[a] Titanium Ti-6Al-4V (Grade 5) [21]

[b] Aluminum 6061-T6 [22]

[c] Toray 2510 Prepreg system, part P707AG-15, using unidirectional T700G carbon fiber [23, 24]

[d] Toray 3900 Prepreg system, part P2362W-19L, using unidirectional T800S carbon fiber [23, 25]

1.3 Discontinuous Fiber Composites

The ability to manufacture discontinuous fiber composites (DFCs) using traditional manufacturing processes like those used by metals allows for lower manufacturing costs and higher fabrication rates than comparable continuous fiber composites (CFCs), which are constrained by the tape laying or filament winding processes employed [26]. As mentioned in section 1.1.3, a discontinuous fiber composite is one comprised of chopped, short fiber strands embedded in a matrix. This key property allows for the use of manufacturing processes and technologies typically seen with metals, such as additive manufacturing where free fibers embedded in a matrix are deposited to build up fiber-reinforced composite parts [27, 28]. Compression molding, sheet molding, injection molding and hot forming may also be employed with carbon fiber platelets to produce parts suitable for secondary structures [9, 19, 26, 29]. Although DFCs typically have lower strength and stiffness than CFCs [19], they still compare well with conventional metal structures formed from titanium and aluminum, as seen in table 1.2. The ability to be formed into complex shapes allows for DFCs to be substituted in place of traditional metal structures like window frames, brackets, fittings, intercostals and others [30], something entirely infeasible with a continuous composite.

Discontinuous fiber composites have a number of material advantages over continuous fiber composites. The heterogeneous, discontinuous nature of the mesostructure allows for greater dissipation of the fracture energy than aluminum alloys and continuous composites, which results in a higher damage tolerance and in some cases an insensitivity to stress raisers such as notches, holes, and other geometrical features [19, 29]. This produces a more desirable pseudo-ductile, progressive failure pattern in contrast to the more brittle fracture behavior of continuous composites [32]. These properties, however, depend greatly on the mesostructure of the material and on the structure geometry, which may vary significantly from part to part. An investigation by Feraboli et al. [33] demonstrated a strong link between the aspect ratio of the platelet and the resulting structural strength, and observed that failure is

Table 1.2: Material properties of TenCate composite compression molding compounds and aerospace-grade metals

Material	Density (g/cc)	T Modulus (GPa)	T Strength (MPa)
Titanium[a]	4.43	114	1100
Aluminum[b]	2.7	68.9	276
MS-1A[c]	1.55	131	290
MS-1H[c]	1.52	69	256
MS-4H[c]	1.52	43	302

[a] Titanium Ti-6Al-4V (Grade 5) [21]

[b] Aluminum 6061-T6 [22]

[c] TenCate chopped-fiber compression molding compounds [31]

matrix-dominated with little to no fiber breakage. Ko et al. [29, 32] found that the fracture energy dissipated by DFCs depends on the platelet size and specimen thickness, with longer platelets and thicker specimens dissipating greater fracture energy. The challenge, however, is that the high scatter in material properties and the unique features of the mesostructure are presently very difficult to capture accurately using numerical modelling [26, 29, 34]. This leads to a situation where in order to certify parts for use on aircraft, an excess of physical testing is necessary [26], as was needed to certify the window frame of the Boeing 787.

1.4 Literature review: Out-of-plane effects and complex geometries

Of more particular interest to this work are the mesostructure features that arise from manufacturing processing conditions and platelet morphologies, and attempting to capture and simulate these using numerical modelling. A review of the literature will be discussed

in this section as pertains to these qualities.

In 2017, Selezneva et al. [34] proposed a numerical model to predict the mechanical properties of randomly-oriented strand (ROS) composites, a type of DFC, the objective being to capture the average strength, elastic modulus, and the range of statistical variation seen in the experimental data. Selezneva's model builds on the work of Feraboli et al. [35] and others to implement a finite element analysis combined with Hashin's failure criteria and a fracture energy based approach to estimate the elastic properties. In order to capture the heterogeneity of discontinuous composite materials, the model uses a virtual specimen that has been discretized into small, representative volume elements (RVE), each with unique fiber layups. This represents a simplification of the mesostructure of ROS composites in order to form a microstructure to provide material properties using classical laminate theory (CLT). Notably, the model does not capture the effect of out-of-plane orientations or interlaminar crack propagation, and delamination as a failure mode is neglected entirely. Selezneva et al. found that increasing the strand length increases the stiffness and elastic modulus, approaching that of a quasi-isotropic (QI) continuous fiber specimen. It was found that strength falls far short (below 50%) of the QI specimen, even as fiber length increases. It was observed that as strand length decreases, a tendency to out-of-plane orientations in the strands leads to a reduction in strength along the loading directions as the through-thickness distance that a crack needs to span to initiate failure is decrease.

This finding as relates to the out-of-plane orientations and decreasing length of strands is supported in 2020 by Alves et al. [36]. A virtual study using a numerical model that produces realistic waviness (out-of-plane behavior), variable fiber volume fractions and variable platelet thicknesses was undertaken. Alves et al. found that shorter, narrower platelets are more prone to out-of-plane orientations than longer, larger platelets, corroborating results in Selezneva et al. [34] and Ko et al. [32]. A parametric study was conducted to examine the effect of carbon fiber tow length and thickness on the elastic modulus, wherein it was

found that tow length was found to be a significant factor in reducing the elastic modulus. Reductions in the elastic modulus up to 25% relative to the QI baseline for platelets as short as 10 mm were observed. By contrast, carbon fiber tow thickness had a more muted effect, with reduction in the elastic modulus increasing from a low of 5% to a high of 10% with increasing thickness. The higher reduction due to tow thickness is primarily a function of increased waviness and out-of-plane orientations in the fibers, as it was observed that discontinuities in the fiber tows are only a small factor, contributing reductions around 6%, whereas waviness is responsible for reducing the elastic modulus by up to nearly 20%. Alves et al. likewise show that their virtual study has good agreement with available experimental data seen in Selezneva et al. [34] and elsewhere.

Regarding the connection between molding processes, platelet orientations, and the resulting distribution of mechanical properties, Sommer et al. [37] conducted flow simulations in combination with finite element analysis (FEA). Simulations with three orientations were undertaken: transversely-dominated, uniformly distributed, and longitudinally-dominated. From these simulations, it was found that the orientation of the platelets is a key driver for mechanical properties. As part of these simulations, a study on the damage mechanisms was carried out, finding that delamination plays a more significant role in the longitudinal specimens than in the transverse specimens, and conversely that local fractures played a more significant role in the transverse specimens than the longitudinal specimens. It was found that delamination correlates with increased fiber alignment, and that the primary failure mode, regardless of platelet alignment, was matrix cracking and platelet disbonding. Fiber breakage was not observed as a main failure mode, as most fiber failures occurred after ultimate load was reached.

1.5 Research Objectives

The main thrust of this work is the investigation and characterization of the effects of platelet morphology and manufacturing-induced flow conditions on the elastic response of discontinuous fiber composites structures. This will be accomplished through the use of mechanical tensile testing of experimental specimens manufactured with two (2) platelet geometries and two (2) manufacturing processes, at three (3) specimen thicknesses. Microcomputed tomography will be employed in order to characterize the relationship between fiber orientation states and flow conditions, and the subsequent impacts on the elastic properties. Micrography will be utilized to qualitatively examine the differences in the resulting composite mesostructure between the flow conditions. The experiment regime will be discussed in chapter 2, with an analysis of the results presented in chapter 3.

The results of the experimental effort will facilitate a virtual study of the complete range of in-plane fiber orientation states, governed through the use of 2nd-order orientation tensors, and provide a foundation for improvements to an in-house numerical modelling solution to enable more robust simulations and support more complex orientation states, to include out-of-plane orientations. The simulation methodologies and the scope of the virtual study are presented in chapter 4, and the results are discussed in chapter 5.

Chapter 2

EXPERIMENTAL CHARACTERIZATION

2.1 Specimen Design, Manufacturing and Preparation

To investigate the effect of platelet morphology and flow conditions on the elastic behavior of DFCs, and to support the development of computer modelling, a series of experiments were undertaken.

2.1.1 Material properties and platelet geometry

The material of choice for this work is APC (PEKK-FC), an aerospace-grade thermoplastic carbon fiber composite system manufactured by Solvay. Consisting of unidirectional continuous fiber reinforcement embedded in a thermoplastic matrix of poly-ether-ketone-ketone (PEKK) [38], APC (PEKK-FC) is shipped as rolls of preimpregnated tape which is then chopped to form the platelets used in the manufacture of the full size panels and fingers. Nominal mechanical properties are presented in table 2.1, and the geometry of the platelets used in the manufacture the specimens are presented in figure 2.1.

2.1.2 Manufacturing

To support investigation into the effect of flow condition on the elastic behavior of DFCs, two (2) manufacturing processes were employed to induce flow effects. Manufactured by SEKISUI Aerospace using a proprietary process, two (2) types of composite structures were prepared from which specimens were cut: low-flow (LF) quasi-isotropic (QI) panels, and high-flow (HF) fingers containing a high degree of flow-induced anisotropy. Examples are

Table 2.1: Material properties of APC (PEKK-FC)

Tensile Modulus		Tensile Strength		
Fiber				**Prepreg Properties**
0°	20.1 Msi	0°	357 ksi	Resin content: 34% by weight
90°	1.5 Msi	90°	8.9 ksi	Fiber: AS4D 12k
Resin				
	0.65 Msi		14.8 ksi	

Manufactured by Solvay, properties reproduced from technical data sheet [39]

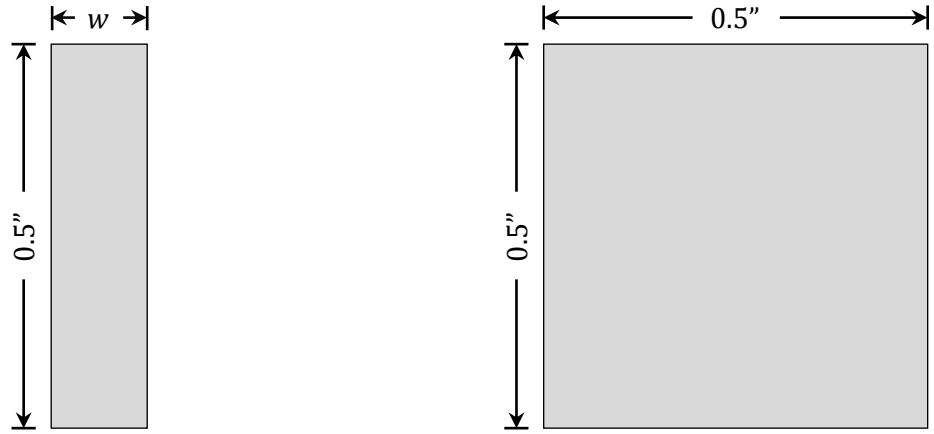

(a) Narrow platelet **(b)** Square platelet

Figure 2.1: Geometry of chopped carbon fiber platelets used in manufacturing

Width of narrow platelet is proprietary; image not to scale

presented in figure 2.2.

(a) Low-flow panel **(b)** High-flow fingers

Figure 2.2: Low-flow molded panels and high-flow molded fingers manufactured by SEKISUI Aerospace, supplied by Boeing

While the precise manufacturing details are proprietary, the Solvay technical data sheet for APC (PEKK-FC) suggests that a typical autoclave consolidation cycle consist of heating a part to 710°F at any ramp rate and holding the part at temperature for 20 minutes at 100 psi. Cooling is advised to not exceed a maximum rate of 20°F per minute while holding a pressure of 100 psi until the temperature falls below 250°F [39]. The panels manufactured for this work were likely prepared under similar conditions.

Low-flow panels at three (3) thicknesses were produced: 0.065", 0.15", and 0.25" using narrow platelets (NP), and 0.065" and 0.15" for square platelets (SP). The 0.25" panels were not manufactured with square platelets due to limited resources. High-flow fingers were produced at 0.15" thickness, using both narrow and square platelets. Table 2.2 contains a summary of the manufactured configurations.

Table 2.2: Geometry of low-flow panels and high-flow fingers manufactured with narrow platelets (NP) and square platelets (SP)

Platelets	Thickness (in)	Width (in)	Length (in)	Form factor
Low-flow panels				
NP/SP	0.065	12	12	Panel
NP/SP	0.15	12	12	Panel
NP[a]	0.25	12	12	Panel
High-flow fingers				
NP/SP	0.15	12	1.5	Fingers

[a] SP not manufactured due to limited resources

2.1.3 Specimen preparations

Specimens were cut using an MK Diamond MK-101 Tile Saw with a 10" diamond-coated continuous rim wet cutting blade from the low-flow panels and high-flow fingers subject to the geometry defined in figure 2.3, in accordance with the ASTM D3039 [40] standard. The total number of specimens produced is included in table 3.1 in chapter 3. Specimen edges and corners were lightly sanded with 100-grit sandpaper to remove burrs and slivers.

Gripping tabs were cut from G-10 grade Garolite sheets at 1/8" and 3/32" thicknesses. The 3/32" thick Garolite gripping tabs were used with the 0.25" thick specimens in order to fit within the grips on the load frames. 1/8" thick gripping tabs were used in all other cases. The contact surfaces on the specimens and on the gripping tabs were sanded with 80-grit sandpaper to create a textured bonding surface. The contact surfaces on the specimens and gripping tabs were then cleaned with acetone, bonded together with J-B Weld Steel

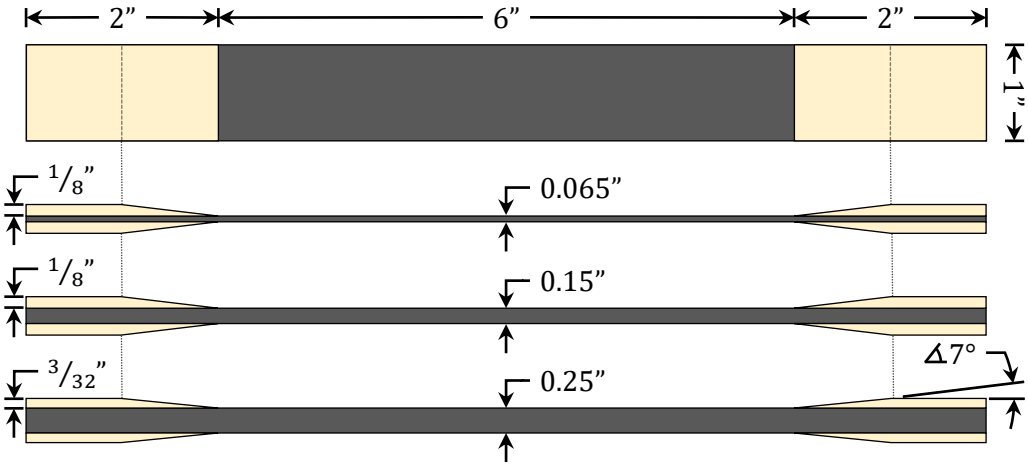

Figure 2.3: Specimen geometry definitions for the three (3) test configurations
3/32” tab used with 0.25” thick specimens in order to fit within load frame grips

Reinforced Epoxy, and then wrapped with masking tape. The tabbed specimens were then clamped with binder clips and quick-grips and the epoxy was allowed to cure over 24 hours at room temperature.

2.1.4 Tensile test preparations

Specimens were prepared for displacement-controlled tensile loading, with digital image correlation (DIC) as the strain measurement mechanism, using a black-and-white speckle pattern (see figure 2.4). The Garolite gripping tabs were wrapped with masking tape to prevent contamination from the spray paint. The front surface across the gauge area was then coated with a white layer of spray paint and allowed to dry, after which a light dusting of black spray paint was applied indirectly at a distance of two-to-three feet to create the speckle pattern. After allowing the paint to dry for 24 hours, masking tape and excess epoxy were removed from the sides of the specimen gripping tabs.

Figure 2.4: Example of DIC speckle pattern applied to specimens
Speckle pattern shown is typical, but specimens are not from this work

2.2 Mechanical Testing

The experimental portion of the research involved the mechanical testing of specimens subject to displacement-controlled tensile loading until failure, with strain data acquired optically with digital image correlation techniques.

2.2.1 Equipment

Tensile tests were conducted initially with an Instron 5580 Series (model 5585H) electro-mechanical, dual-column, floor mounted axial load frame with a 250 kN (56.2 Klbf) load cell. Mitigation of a systemic issue that was observed with the Instron 5585H was implemented after the Shore Western load frame purchased by the University of Washington could be installed and calibrated. More details on the nature of the issue are presented in chapter 3, section 3.1.2. Completion of the remainder of tensile testing was conducted with a Shore Western 306 Series (model 306.4) hydraulic, dual-column, floor mounted axial/torsional load frame with a 500 kN (100 Klbf) load cell.

An AF Micro-NIKKOR 200mm f/4D IF-ED lens with a 200mm focal length, and a Sigma

135mm F1.8 DH HSM Art lens with a 135mm focal length were used in combination with a Nikon D5600 Digital SLR. Data was saved as 6000×4000 pixel JPEGs without compression to a class 10 SanDisk Extreme SDXC SD card with a write speed of 150 MB/s.

2.2.2 Test setup

The equipment was setup with the camera on a tripod between four-to-ten feet from the specimen, with the lenses manually focused on the gauge area. Lens focus was checked between tests and recalibrated as necessary to ensure clear and accurate images. A NEEWER PT-176S LED photo/video light emitting bright, white light was clamp-mounted to the load frame and directed to the visible face of the specimen (see figure 2.5). Prior to mounting a specimen in the load frames, a steel plate was inserted and the grips clamped in order to eliminate torsional effects.

Specimens were placed in the fixtures on the load frame and the fixed grip clamped. The crossbar on the load frames were then moved vertically into position, and the load tared. The grip on the crossbar was then clamped to the specimen. Displacement data was acquired at 10 Hz via electronic measurement provided by the load frames, and DIC data at 1 Hz via the camera system, begun nearly simultaneously (± 2 seconds) with any misalignment in the data corrected during post-processing by detection and alignment of the fracturing event. Note that DIC data were acquired for one face of the specimen only, which Tang et al. [41] have found to be sufficient for observing strain localization coinciding with failure initiation and the determination of elastic properties.

Data were exported in file formats particular to the software for a given load frame, and then transferred by USB to personal computers and cloud-based file storage. Measurement units and file formats were standardized in post-processing.

(a) Setup with Instron 5585H **(b)** Setup with Shore Western 306.6

Figure 2.5: Setup of tensile test equipment and DIC data acquisition system

2.2.3 Test parameters

Specimens were subject to displacement-controlled loading until failure in accordance with the ASTM D3039 standard. A ramp rate of 2 mm/s was used with the Instron 5585H load frame, and a ramp rate of 1 mm/s was used with the Shore Western 306.4 load frame. This change in ramp rate is a result of abnormalities with the observed rate of strain application in the Instron 5585H, which were not present with the Shore Western 306.4, and will be discussed in detail in chapter 3, section 3.1.2.

2.3 Microcomputed tomography

Microcomputed tomography was employed in order to examine the fiber orientation states within a subset of the experimental test specimens. After non-destructive scanning was completed, specimens were subject to tensile testing as outlined in section 2.2.

2.3.1 Key concepts regarding fiber orientation states

In order to understand the role of micro-CT scanning in the determination of fiber orientation states, the following concepts are of significant import.

The probability density function (PDF) ψ serves as the most general and complete description of a fiber orientation state over a given region within a composite structure, with properties described and defined in Advani and Tucker [42]. This description, however, is verbose, and difficult to utilize in numerical modelling. From their work, ψ may be represented in terms of the unit orientation vector $\bar{p}$, which describes the orientation state of a singular carbon fiber strand.

Using the definitions from Advani and Tucker [42], equations 2.1-2.3 define the relationship of the vector components p_i to the in-plane angles θ and out-of-plane angles ϕ. Figure 2.6 defines the relationship of $\bar{p}$ to the coordinate system of the specimen, with the 1-2 plane parallel to the face, and the 1-direction aligned with the longitudinal axis.

$$p_1 = \sin\phi\cos\theta \tag{2.1}$$

$$p_2 = \sin\phi\sin\theta \tag{2.2}$$

$$p_3 = \cos\theta \tag{2.3}$$

A more concise description of the fiber orientation state employs the use of even-ordered orientation tensors. The 2nd-order orientation tensor may be calculated through the use of the integration of unit orientation vectors weighted by the probability density function $\psi(\bar{p})$:

$$a_{ij} = \oint p_i p_j \psi(\bar{p}) d\bar{p} \tag{2.4}$$

This produces a symmetric tensor with six (6) unique terms that are diagonally dominated. The diagonal terms a_{ii} are used to describe the longitudinal, tranverse, and out-of-plane fiber orientation states respectively.

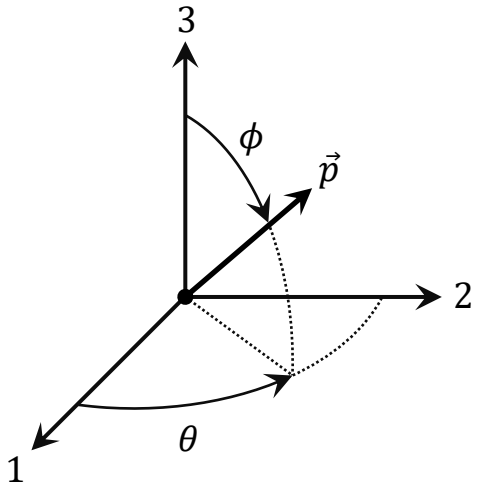

Figure 2.6: Coordinate system and definitions for in-plane angle θ, out-of-plane angle ϕ and the unit orientation vector $\bar{p}$

2.3.2 Acquisition of micro-CT data

A North Star Imaging X-View X5000 Computed Tomography System was employed to produce micro-CT scans for a subset of each specimen configuration. A nominal resolution of 26 μm was used to acquire the 2D slices from which a 3D image was assembled. A Gaussian filter utilizing Eigen-analysis was employed to calculate the unit orientation vectors (equations 2.1-2.3) throughout the specimens at each voxel point, written and implemented in Python. Global coordinates were corrected through determination of the edge of the specimen to align the orientations to the reference axes of the specimen, and not the scanner. Calculation was conducted on the University of Washington's Hyak high-performance compute clusters Mox and Klone.

2.4 Micrography

In order for an examination of the mesostructure to be conducted, small 1" slices were cut from the low-flow panels and high-flow fingers to provide samples for evaluation. The slices were encased in epoxy pucks using Allied High Tech's QuickCure Acrylic. Epoxied samples were polished in a Streurs RotoPol 21 and RotoFoce 3 auto-polisher. Following polishing, an Olympus BX50 microscope was used with a magnification of 5× to conduct the inspection of the mesostructure. As of this writing, samples have been prepared for the narrow platelet specimens, and polishing and microscopic evaluation of the square platelets specimens is underway.

Chapter 3
EXPERIMENTAL RESULTS AND ANALYSIS

In this section, an analysis of the elastic modulus of specimens manufactured with either narrow or square platelets with a low-flow or high-flow process will be discussed. Orientation tensors and the fiber orientation distributions within micro-CT scanned specimens will be characterized. A qualitative examination of features within the mesostructure obtained through micrography will be presented.

3.1 Elastic properties

3.1.1 Data reduction and analysis methodology

Load and displacement data from the Instron 5585H and Shore Western 306.4 were processed using MATLAB [43, 44, 45] to standardize units and formatting. Data were reduced by averaging within each second to a time step of 1 Hz, down from a nominal rate of 10 Hz. Discrete time steps at higher frequencies (e.g. 14 Hz) for tests conducted with the Instron 5585H were observed within the load data for a given test, but were not typical, even within that test. Peak load and displacement values were detected and preserved for the second during which they occurred, and were not averaged down. Processed load and displacement data at 1 Hz time steps were exported in a unified format for further processing in MATLAB.

DIC image data obtained at a time step of 1 Hz from the Nikon D5600 Digital SLR camera were pre-processed in MATLAB to remove any trace off-axis rotation of the specimen with respect to the frame of the image, and to crop out extraneous image data. Image data were then ingested into GOM Correlate Pro 2019 [46] for strain and displacement analysis.

Evaluation of average strain and relative displacement at each time step over the face of each specimen was conducted using a grid of equidistant points with 0.1" spacing, allowing for 10 points across the width and typically 56-60 points lengthwise over the visible length of the gauge area. Occasionally, the clamps of the load frame obscured the top and bottom edges. Strain and displacement data at 1 Hz time steps were exported in tabular format for further processing in MATLAB.

Processed load, displacement, and strain data were then imported into MATLAB, and elastic properties and related statistics were calculated in accordance with the ASTM D3039 standard. As part of this process, a routine to detect fractures in the load data and the DIC data was used to correct temporal misalignment (0-1 seconds was typical, with values up to 5 seconds observed).

Table 3.1 contains the complete set of planned and completed tests for narrow platelet low-flow (NP-LF) and high-flow (NP-HF) specimens and square platelet low-flow (SP-LF) and high-flow (SP-HF) specimens. Square platelet panels at 0.25" thicknesses were not manufactured due to a lack of available resources and modifications to immediate test priorities. The focus of this analysis will be on the 0.15" thick specimens, but the complete set of available data will be presented and discussed.

3.1.2 Systemic issues with the Instron 5585H

During data reduction and analysis of the Instron 5585H load data, a number of systemic issues were exposed. Figure 3.1 presents the qualitative trends in the load data and DIC displacement data acquired from the load frame. The mitigation steps taken in response to these systemic issues were to conduct the remaining balance of tests with the Shore Western 306.4 load frame, which was initially unavailable at the time tests began on account of being recently purchased and not yet calibrated. Data in the following figures have been normalized to preserve the proprietary experimental data and to allow direct, qualitative comparisons.

Table 3.1: Number and types of specimens subject to tensile loading

Thickness (in)	Planned	Completed	Non-viable[a]
NP-LF			
0.065	22	17[b]	0
0.15	33	33	3
0.25	33	33	2
SP-LF			
0.065	20	15[b]	0
0.15	30	30	0
NP-HF			
0.15	12	12	0
SP-HF			
0.15	12	12	0

[a] Errors in acquisition of the DIC data rendered the data unusable

[b] Technical challenges with micro-CT scanning of thin specimens are unresolved

For this discussion of the systemic issues, samples are presented from the NP-LF 0.25" thick data set, but the issues are present in all tests conducted with the Instron 5585H load frame. Specifically, the primary observations are an extended specimen relaxation time as shown in figure 3.1a and oscillations in the DIC displacement data as shown in figure 3.1c. It was also observed that time-to-fracture with a ramp rate of 2mm/s using the Instron 5585H was, on average, 3× to 4× longer than time-to-fracture on the Shore Western 306.4. The source of the oscillations seen in the DIC displacement data are unclear, but may be related to vibrations in the building transmitting up the camera tripod to the lens. It is noted that this extended relaxation period is entirely absent in the data acquired from the Shore

Western 306.4, as are the oscillations seen in the DIC displacement data from the Instron 5585H.

Crucially, as the oscillations are uniform, in that the entire set of tracking points move as a group, the relative displacements are preserved and the strain measurements over the gauge area from tests conducted on the Instron 5585H are still meaningful. While the difference in the absolute displacement between the Instron 5585H and Shore Western 306.4 as seen in figures 3.1c and 3.1d is significant, the relative displacements across the gauge area are similar. The net effect of these systemic issues in the Instron 5585H are an increase in the noise and scatter of the data, as seen in figure 3.2. The stress/strain curves are smoother and the slopes more consistent in tests conducted with the Shore Western 306.4 as compared with the Instron 5585H.

On average, the elastic modulus calculated from data obtained from the Instron 5585H is 2.7% lower, and the standard deviation is 57% larger, than for data from the Shorn Western 306.4, as seen in figure 3.3. In spite of these issues, in general, the calculations of the elastic modulus agree between tests conducted with the Instron 5585H and those conducted with the Shore Western 306.4, allowing the more detailed analysis that follows.

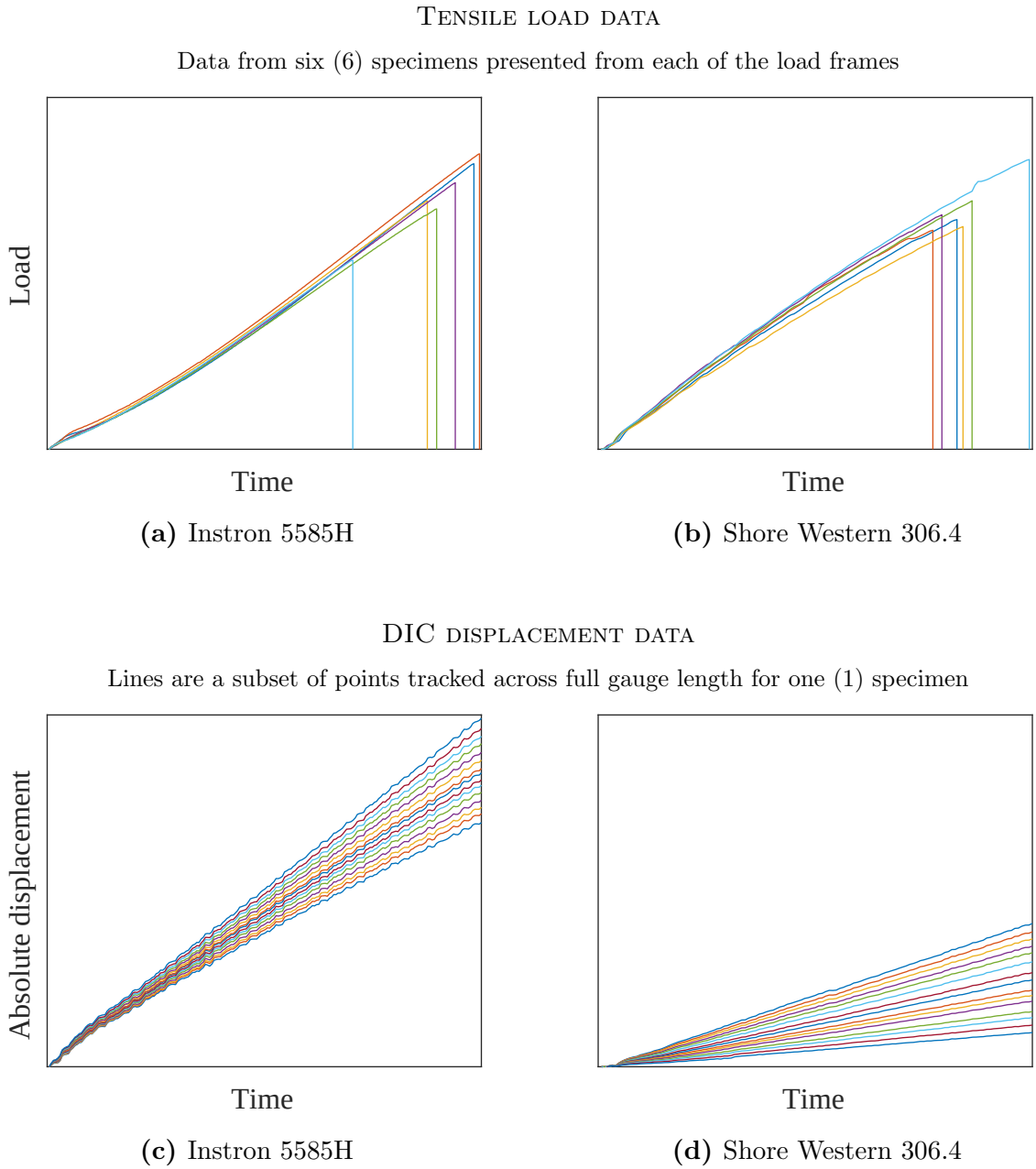

(a) Instron 5585H **(b)** Shore Western 306.4

(c) Instron 5585H **(d)** Shore Western 306.4

Figure 3.1: Extended relaxation and oscillations in data acquired from Instron 5585H mitigated by switching to Shore Western 306.4.

Data sampled from NP-LF 0.25" thick specimens, but observations are typical

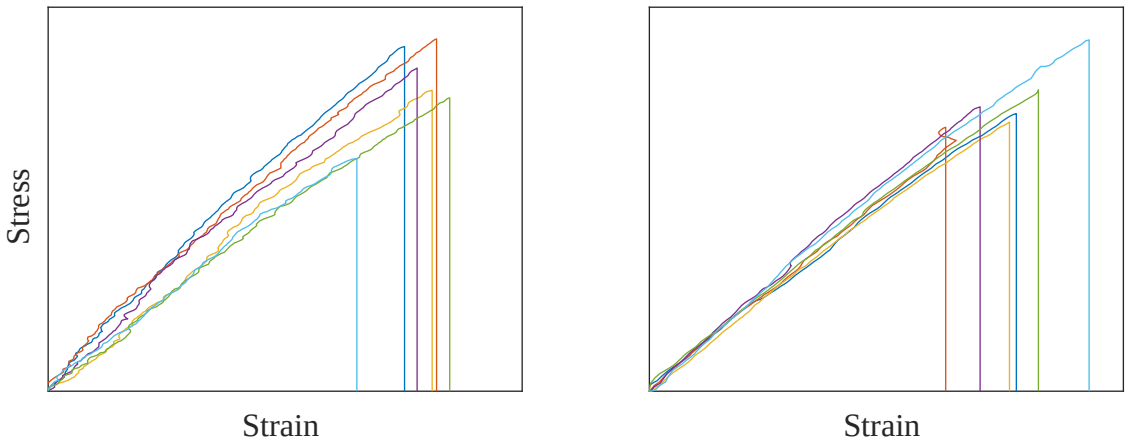

(a) Instron 5585H **(b)** Shore Western 306.4

Figure 3.2: Increased noise, scatter in stress/strain curves in data from Instron 5585H mitigated by switching to Shore Western 306.4.
Data sampled from NP-LF 0.25" thick specimens, but observations are typical

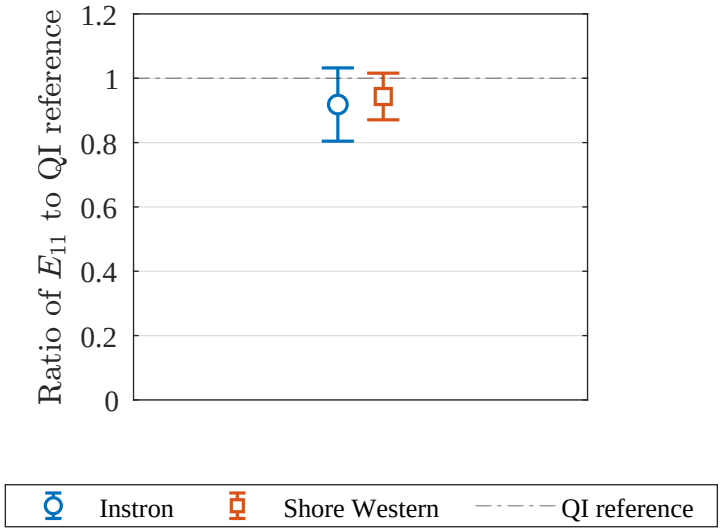

Figure 3.3: Increased scatter observed in the elastic modulus in data acquired from Instron 5585H as compared to Shore Western 306.4.
Data sampled from NP-LF 0.25" thick specimens, but observations are typical

3.1.3 Elastic modulus

The elastic modulus values presented in this subsection have been normalized against the elastic modulus of a quasi-isotropic (QI) continuous fiber composite reference specimen of the appropriate dimensions, to preserve proprietary experimental data. Table 3.2 contains the mean modulus, standard deviation and coefficient of variation (CoV) as determined following the ASTM D3039 standard.

Table 3.2: Experimentally measured elastic modulus E_{11}

	Elastic Modulus		
Thickness (in)	Mean[a]	St. Dev[a]	CoV (%)
NP-LF			
0.065	0.906	0.108	11.95
0.15	0.896	0.114	12.71
0.25	0.934	0.090	9.61
SP-LF			
0.065	0.781	0.090	11.50
0.15	0.815	0.058	7.16
NP-HF			
0.15	1.038	0.086	8.31
SP-HF			
0.15	1.008	0.055	5.40

[a] Data has been normalized against quasi-isotropic values

From the available results, it may be observed that the thickness of the specimen has negligible effect on the elastic modulus. Figure 3.4 suggests that for square platelets, thick-

ness has a small effect on the elastic modulus, with increasing thickness leading to a 4.4% increase in modulus from 0.065" to 0.15". For the narrow platelets, the modulus is very nearly constant across thicknesses, decreasing by 1.1% from the 0.065" to 0.15" thick specimens, before increasing by 4.2% from the 0.15" to 0.25" thick specimens. Though for square platelets the standard deviation decreases by 36% with increasing thickness, and the same is true for narrow platelets with a 21% decrease in the standard deviation from 0.15" to 0.25" thick specimens, the increase in thickness for narrow platelet specimens from 0.065" to 0.15" shows an increase of 5.6% in observed standard deviation. Ko et al. [29] found a thickness effect for the fracture energy, and it stands to reason given the complex mesostructure of DFC structures, thickness may be a meaningful factor in characterizing the variability in elastic response of DFC specimens. More investigation is needed, as the scatter of the data is quite large (see figures A.1-A.3 in appendix A), to definitively establish the effect of thickness on the elastic modulus and the associated scatter.

With respect to platelet morphology, it may be observed in figure 3.4 that square platelets consistently underperform the narrow platelets, respecting the elastic modulus, by an average of 13.3% relative to the quasi-isotropic (QI) reference. Square platelets have a relative difference of 22.5% from the QI reference, and narrow platelets a relative difference of 9.2%. This is in contrast to the results suggested in Alves et al. [36] which found a 5% to 25% reduction in elastic modulus in shorter, narrower platelets as compared with longer, wider platelets. Given that the square and narrow platelets share a length, it is speculated that the mitigating factor is the width. It has been found in Nakagawa et al. [47], and in mesostructure simulations as will be discussed in chapter 5, that two factors may be at work. First, when platelets are layered, if the number of platelets through the thickness is below the average within a specimen, there is a decrease in the local fiber volume fraction and the area saturates with resin, as seen in figure 3.5. Second, the larger aspect ratio of the square platelets leads to an increase in voids and resin rich areas in mesostructure simulations. These two factors

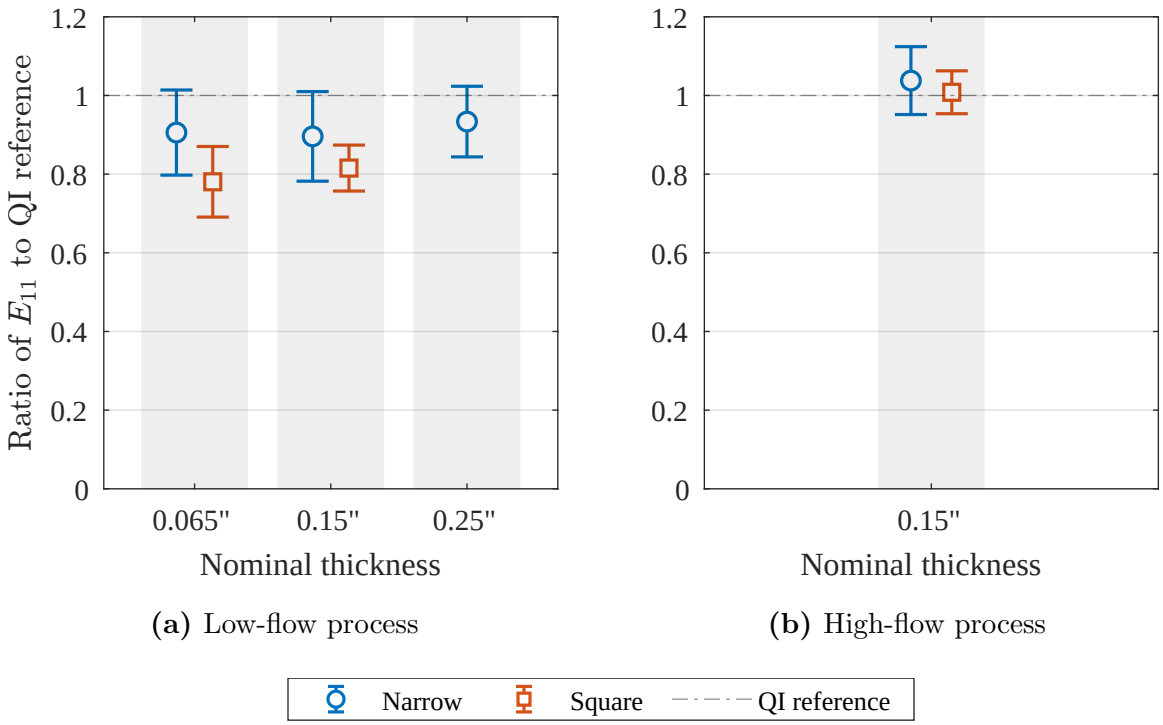

Figure 3.4: Response of elastic modulus E_{11} to platelet morphology grouped by flow condition and nominal specimen thickness

could account for the reduction in elastic modulus as compared with the narrow platelets, which may pack more densely during the molding process.

As concerns the standard deviation, square platelets provide consistently lower scatter than the narrow platelets, with a relative difference of 18.2% to 65.1% lower for 0.065" and 0.15" thick low-flow specimens respectively, and 44.0% for high-flow specimens. This effect holds true for flow condition as well, with high-flow specimens showing a lower standard deviation in the elastic response than the low-flow conditions with a relative difference of

18.9% and 29.5% for narrow and square platelet specimens respectively, as seen in figure 3.4. Scatterplots comparing flow condition are available in figures A.5 and A.6 in appendix A. This suggests that though square platelets have a lower elastic modulus on average, the material response is more consistent than narrow platelets, which may be an acceptable trade off for some applications.

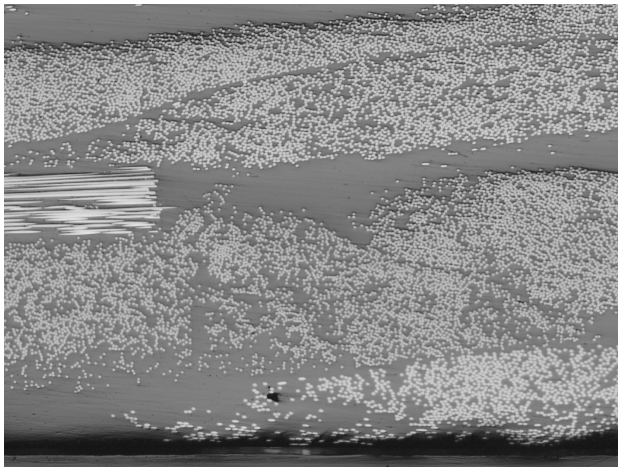

Figure 3.5: Increase in platelet thickness caused by lack of platelets when compared to the average number of platelets through the thickness
Reproduction of figure from unpublished work by Nakagawa et al. [47]

This tendency of square platelets to have lower elastic modulus than the narrow platelets is mitigated by flow condition, as seen in figure 3.6, where high-flow square platelet specimens are only marginally lower than high-flow narrow platelet specimens (2.9% relative difference versus 14.8% and 9.5% in the comparable low-flow specimens, see table 3.2) as compared with the low-flow specimens.

It is also observed that high-flow specimens have an elastic modulus that exceeds the QI specimens along the loading direction by 3.7% and 0.8% for narrow and square platelet specimens respectively. Likewise, the high-flow elastic modulus is significantly higher (12.9%

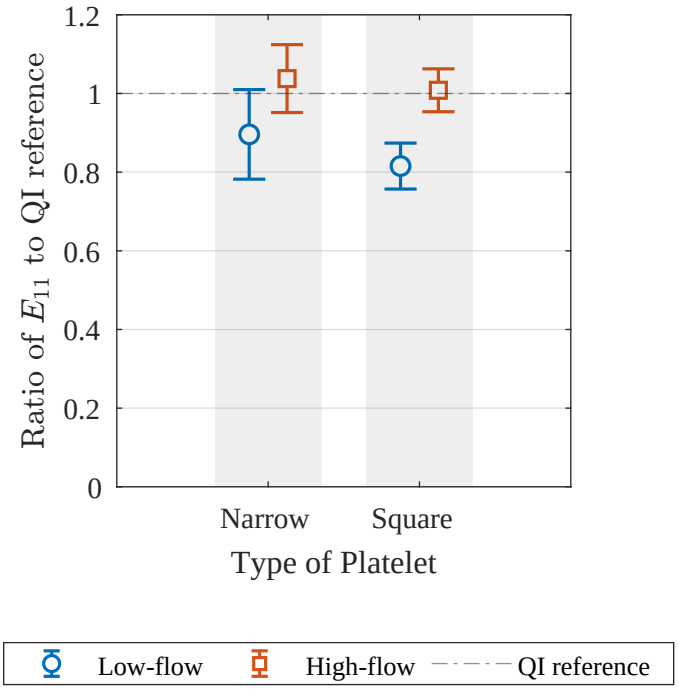

Figure 3.6: Response of elastic modulus E_{11} to flow condition grouped by platelet morphology for nominally 0.15" thick specimens

and 23.3% for NP/SP respectively) than that of the low-flow specimens. It may be concluded that the high-flow manufacturing process introduces favorable fiber alignment along the loading direction as has been shown in Sommer et al. [37], which is advantageous for tailoring DFC parts to specific use cases in industry. However, it is expected that there is a reduction in the transverse elastic modulus E_{22} commensurate with the increase in the longitudinal elastic modulus E_{11}, but this has not been explored experimentally in this work. Additionally, Alves et al. [36] and Selezneva et al. [34] have shown that increased flow leads to an increase in fiber waviness and magnifies the out-of-plane effects, which has a detrimental effect on

the elastic modulus and fracturing behavior. Micrographs that show this change in fiber orientation behavior from low-flow to high-flow in narrow platelet specimens are presented in section 3.4.

3.2 Orientation tensors

3.2.1 Regarding very thin specimens

A note regarding the 0.065" thick specimens: this thickness is below the minimum thickness recommended by the manufacturer, and experiments were conducted largely to explore the effects of producing a part with geometry at the very edge of reasonable. Micro-CT scanning has been challenging, with specimens warping when placed in fixtures. Data is included for completeness, but results may not be indicative of meaningful trends.

3.2.2 Calculation of the orientation tensors

Utilizing the end product of the analysis steps conducted in chapter 2, section 2.3, a 2nd-order orientation tensor was calculated for each specimen using equation 2.4. $\psi(\bar{p})$ is treated in these equations as 1 given the data is an explicit measurement of the fiber orientation distribution as it exists in the micro-CT scanned specimens, and the integral is conducted over the entire set of voxels. The results of these calculations for the diagonal terms of the orientation tensor are presented in section 3.2.3.

3.2.3 Analyses of the orientation tensors

The results obtained from the micro-CT analysis as pertaining to the orientation tensors are presented here in table 3.3. It is observed that for the low-flow condition, the average values of the a_{11} and a_{22} terms are within 1-5%, excepting the 0.065" thick NP specimens (17%), for which scans are less reliable, suggesting a near-uniform distribution as will be shown in section 3.3.2. The a_{11} terms for the high-flow condition are significantly higher (52% on

average) than the a_{22} terms, indicating greater fiber alignment along the longitudinal axis. Similarly, the a_{33} terms are 54.5% larger on average in the high-flow condition than the low-flow condition, indicating an increased out-of-plane effect induced by the manufacturing process.

Table 3.3: Orientation tensor terms a_{ii} for micro-CT scanned specimens

	a_{11}		a_{22}		a_{33}	
Thickness (in)	Mean	CoV (%)	Mean	CoV (%)	Mean	CoV (%)
NP-LF						
0.065	0.455	8.08	0.542	6.78	0.00275	10.41
0.15	0.485	4.78	0.510	4.59	0.00504	7.96
0.25	0.494	3.98	0.500	3.92	0.00546	5.87
SP-LF						
0.065[a]	-	-	-	-	-	-
0.15	0.486	9.16	0.511	8.63	0.00322	16.18
NP-HF						
0.15	0.634	5.84	0.358	10.20	0.00748	17.94
SP-HF						
0.15	0.616	7.67	0.377	12.41	0.00693	13.49

[a] Technical challenges with micro-CT scanning of thin specimens are unresolved

There is a noticeable trend with the coefficient of variations for a_{11}, a_{22} and a_{33} within the low-flow condition: as the specimen thickness increases for the narrow platelet specimens, the standard deviation becomes lower, suggesting that specimen mesostructure is increasingly

stable at greater thicknesses, an effect studied in more detail in Ko et al. [29].

3.3 Fiber orientation distributions

3.3.1 Calculation of in-plane and out-of-plane fiber orientation distributions

In order to determine the fiber orientation distributions throughout the specimens, equations 2.1-2.3 were reformatted in order to calculate the angles θ and ϕ, as follows:

$$\theta = tan^{-1}\left(\frac{p_2}{p_1}\right) \tag{3.1}$$

$$\phi = cos^{-1}(p_3) \tag{3.2}$$

These calculations were applied to each array of unit orientation vectors, and the probability distributions were calculated using the `histogram` function in MATLAB with a bin width of 1, across the ranges $\theta \in [-90, 90]$ and $\phi \in [0, 180]$. For the figures in section 3.3.2, a subset $\phi \in [60, 120]$ is presented, as outside of these ranges the probability is equivalently or approximately zero, and not of interest.

3.3.2 Analysis of fiber orientation distributions

The effects of manufacturing flow conditions on the fiber orientation distributions are presented in figure 3.7, and the effects of platelet morphology on the same in figure 3.8.

It is observed that the in-plane fiber orientation distributions for the low-flow condition, as seen in figure 3.7a, are very nearly uniform, regardless of platelet morphology, as was indicated by the orientation terms $a_{11}, a_{22} \approx 0.5$ as discussed in section 3.2.3. The high-flow in-plane fiber orientation distributions seen in figure 3.7c have a higher peak along the loading direction, and deeper minimums along the tangential direction, which supports the more highly-aligned orientation state indicated by the increased a_{11} terms as compared

with the low-flow specimens, and the measured elastic modulus that exceeds that of the quasi-isotropic reference.

The low-flow out-of-plane fiber orientation distributions tend to be sharply aligned with the in-plane direction as seen in figure 3.7b, peaking around a probability of 13% and 18% for the narrow and square platelets respectively. The out-of-plane alignment of fiber orientations in high-flow specimens by contrast is significantly increased in square platelet specimens, with a peak at 90° nearly 38% lower than in the low-flow condition, as seen in figures 3.8b and 3.8d. By contrast, narrow platelet specimens are only slightly more disposed to out-of-plane alignments in a high-flow condition, with a peak at 90° only 12% lower than in a low-flow condition. A lower, wider probability distribution indicates greater likelihood for fiber orientations that are out-of-plane. This supports an observation in section 3.4 regarding increased waviness in high-flow specimens as compared with low-flow specimens.

As concerns platelet morphologies, the gap between narrow and square platelet specimens in the low-flow out-of-plane fiber orientation distribution is quite pronounced, with square platelet specimens being 28% less likely to produce out-of-plane alignments than narrow platelet specimens. This supports a finding by Alves et al. [36] that shorter, narrower platelets are more prone to out-of-plane orientations than longer, wider platelets. It is noteworthy that this tendency is not seen in the high-flow out-of-plane fiber orientation distributions seen in figure 3.7d, where the probability distributions are nearly identical between narrow and square platelet specimens with a relative difference of 1.8% at the peak. This suggests that the effects of flow condition in a high-flow process are dominant, completely overshadowing platelet morphology as concerns out-of-plane orientations. The in-plane high-flow fiber orientation distributions by contrast have a modest gap, with narrow platelets more likely to align with the flow than square platelets by 8.3%.

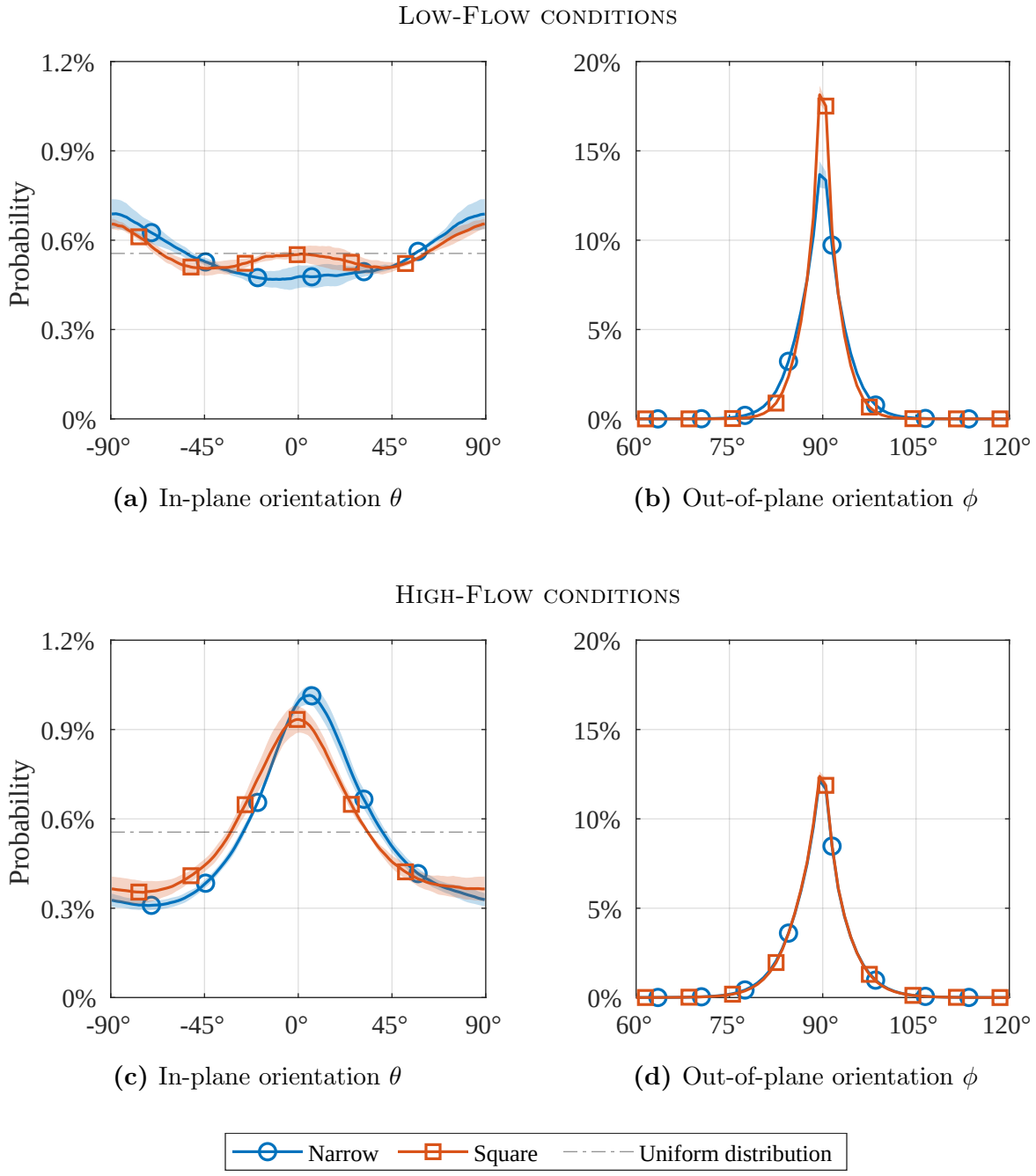

(a) In-plane orientation θ

(b) Out-of-plane orientation ϕ

(c) In-plane orientation θ

(d) Out-of-plane orientation ϕ

Figure 3.7: Comparison of the effect of platelet morphology on the mean fiber orientation distributions for low-flow and high-flow specimens

Shaded bands represent one (1) standard deviation from the mean

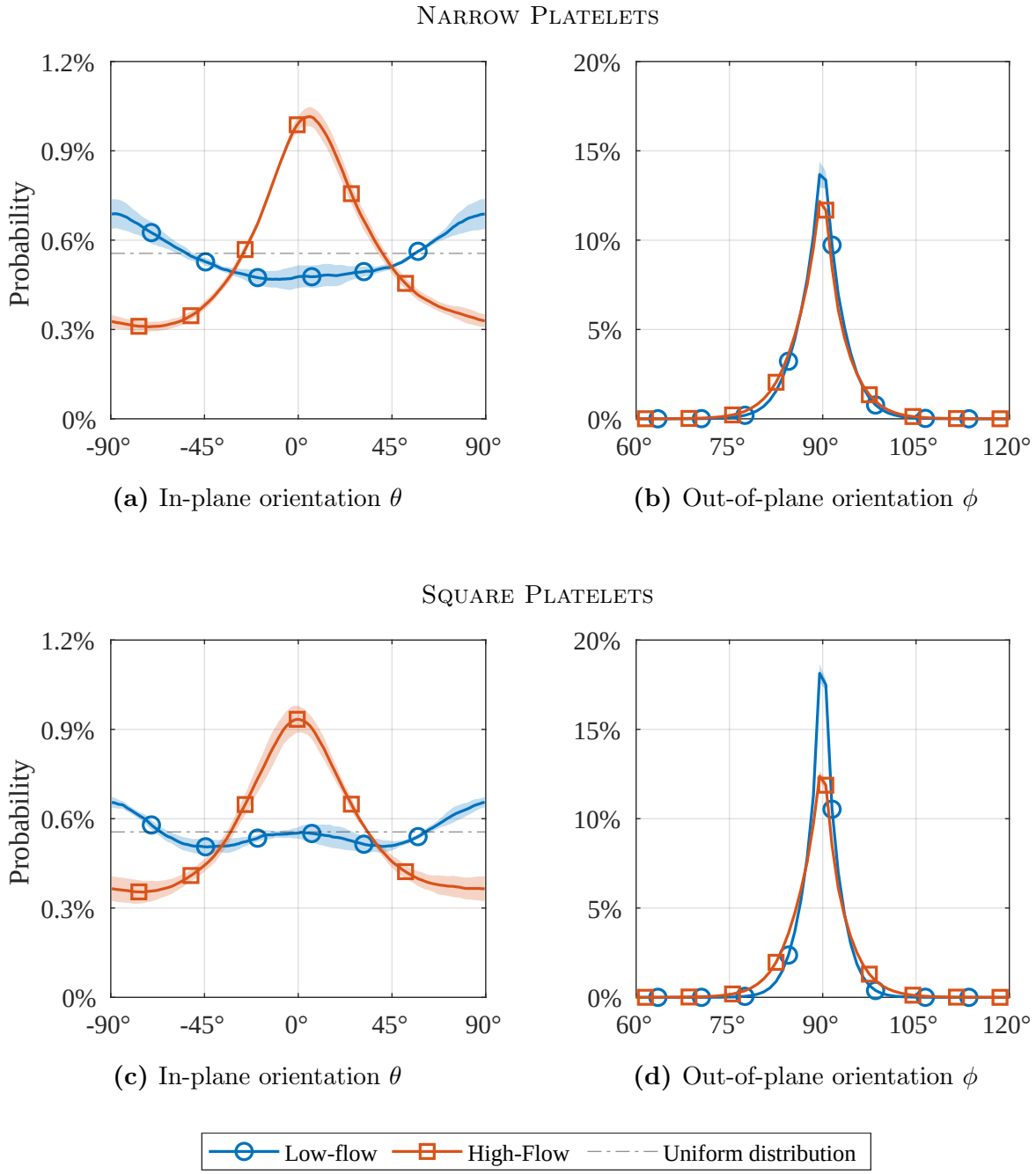

(a) In-plane orientation θ

(b) Out-of-plane orientation ϕ

(c) In-plane orientation θ

(d) Out-of-plane orientation ϕ

Figure 3.8: Comparison of the effect of flow conditions on the mean fiber orientation distributions for narrow and square platelet specimens

Shaded bands represent one (1) standard deviation from the mean

3.3.3 Comparison with recovered fiber orientation distributions

The mode shapes of the in-plane distributions bear a striking resemblance to the probability density functions recovered by numerical approximation techniques from orientation tensors by Chen et al. [48], using methodologies proposed by Advani and Tucker [42]. The minimum around 0° and the peaks around ±90° are similar to those seen in figure 6 (b) from Chen et al., reproduced in figure 3.9. There appears to be qualitative agreement between the experimentally observed results and the numerically derived probability density functions, as the mode shapes seen in the test results for the low-flow condition are similar to those predicted by the Gauss error function from Chen et al. for $0.4 \leq a_{11} \leq 0.5$, as seen in figure 3.10. The same is true for the peaks of the mode shape for the high-flow condition seen in figure 3.7c, and the associated a_{11} values for the experimental fiber orientation distributions fall between the expected ranges of the a_{11} values for the simulated fiber orientation distributions.

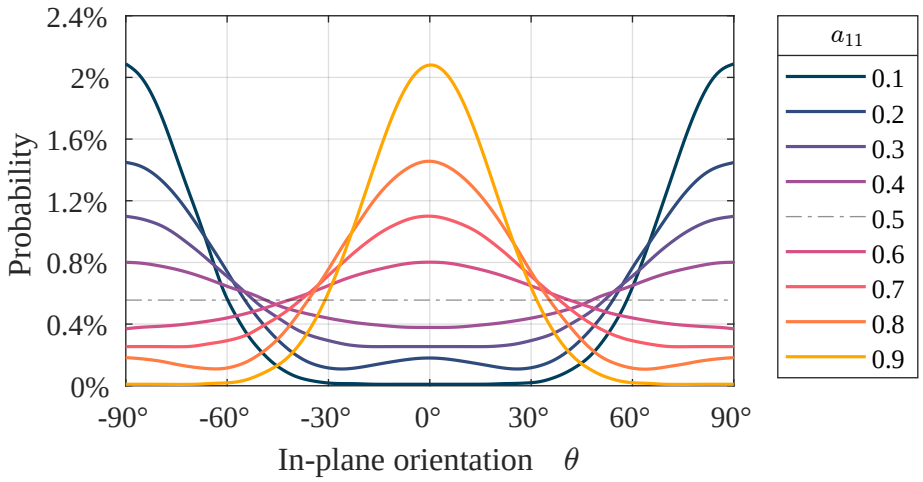

Figure 3.9: Probability density functions (PDFs) of the fiber orientation distributions represented by the Gauss error function

Reproduction of figure 6 (b) from Chen et al. [48]

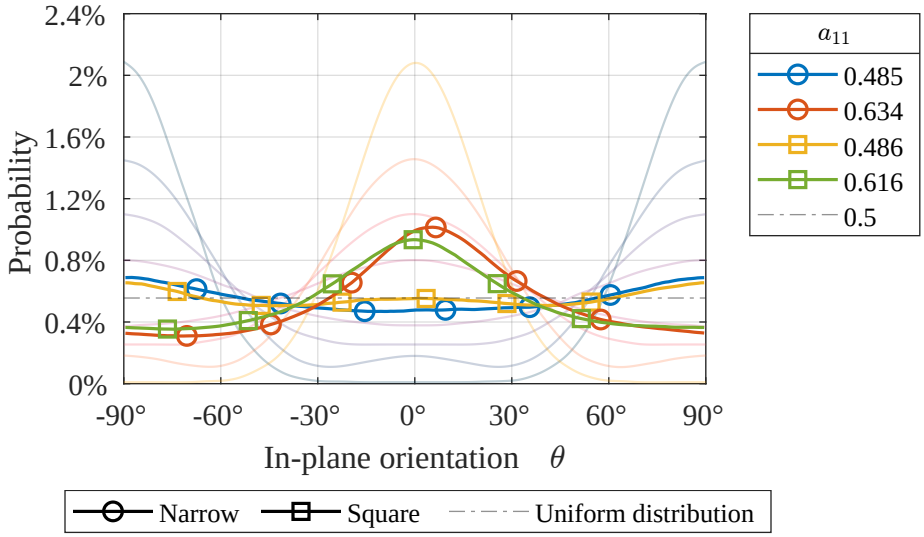

Figure 3.10: Probability distributions from empirical observations with overlay of PDFs represented by the Gauss error function.

3.4 Micrography

Examination of the slices obtained via microscope allows for a comparison of the features of the mesostructure of a low-flow and a high-flow specimen. The samples presented in figure 3.11 are from those manufactured using narrow platelets. Samples for specimens manufactured from square platelets are currently being processed, and were not ready at the time of writing.

The most significant difference between the low-flow and high-flow narrow platelet samples are the presence of extensive porosity throughout the entire width and thickness of the slice. This porosity is not present in the low-flow sample, and so it may be concluded that the process used to form the high-flow specimens is trapping air, creating voids. Resin pockets are present in the both the low-flow and high flow samples. Additionally, the edges of platelets in the low-flow slice are clear and distinct, with each layer easily separable from the next. The same is not true in the high-flow slice, where platelet boundaries are difficult to determine and one platelet has extensive crossover with the next, a function of the turbulence induced during the flow process.

It may also be noted that while both samples display fiber waviness, the waviness is more accentuated in the high-flow specimen. The out-of-plane effects documented by Alves et at. [36] and Sommer et al. [37] are affirmed by these results, and the experimental results discussed above quantitatively described the increased presence of those effects with the lower, wider fiber orientation distribution curves seen in figure 3.7 for the high-flow condition.

(a) NP-LF

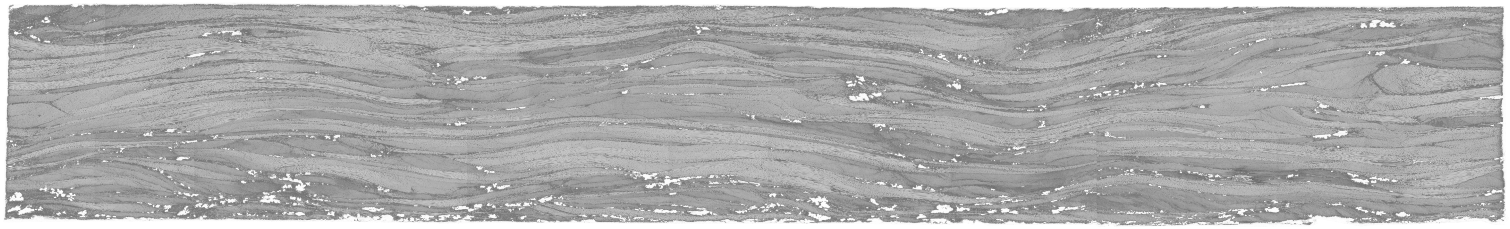

(b) NP-HF

Figure 3.11: Micrographs of typical narrow platelet, low-flow and high-flow specimens

Chapter 4
SIMULATION METHODOLOGY

The experimental test regime undertaken by this work is necessarily restricted to a finite set of manufacturing processes and constrained by the available resources. In order to more broadly characterize the effect of platelet morphology and flow condition over a wider range of inputs, an in-house explicit mesostructure generation algorithm was employed. The workings of the algorithm, the underlying assumptions and the constraints are presented here. Optimizations performed in order to meet the demands of the investigation are detailed. Information pertaining to revisions in the underlying assumptions to expand the functionality and improve the model in the future are discussed in section 4.5.

4.1 Simulation design overview

A parametric study of the effect of in-plane fiber orientation states was conducted using an in-house explicit modelling solution that simulates the mesostructure of rectangular DFC specimens.

The fiber orientation state of the simulation regime is determined by the a_{11} term of a 2nd-order orientation tensor. The sweep of in-plane fiber orientation states involved the input of 101 evenly spaced, discrete a_{11} terms, for $a_{11} \in [0, 1]$, an effective spacing of 0.01. Initially, twelve (12) unique specimens were planned to be generated at each discrete step, and the elastic modulus calculated using finite element analysis for each specimen, for a total of 1,212 simulations for each of the six (6) configurations, in order to capture the scatter in elastic properties typical of DFC structures. However, after completion of the first sweep it was observed that the scatter in the simulation data was not large, and it was determined

that six (6) unique specimens were sufficient to qualitatively capture the scatter of the elastic properties arising from the simulated mesostructure.

Simulations were conducted at three (3) thicknesses, 0.065", 0.15" and 0.25", using both narrow and square platelets with geometry as defined in figure 2.1, for six (6) total configurations. Table 4.1 contains a summary of the completed simulation regime. A detailed discussion of the mesostructure generation algorithm employed in this work is undertaken in section 4.2, and the finite element analysis conducted using the output of that algorithm is discussed in section 4.3.

Table 4.1: Planned simulations for sweep of in-plane fiber orientation states

Thickness (in)	Simulations per a_{11}	Total Simulations
Narrow platelets		
0.065	6	606
0.15	12[a]	1212
0.25	6	606
Square platelets		
0.065	6	606
0.15	6	606
0.25	6	606

[a] Twelve (12) simulations originally planned, but six (6) was determined to be sufficient

4.2 Mesostructure generation algorithm

4.2.1 Overview

The algorithm, in brief, models a laminate with a given fiber orientation state as controlled by the a_{11} term of a 2nd-order orientation tensor. A laminate is built up layer-by-layer, platelet-by-platelet, until the desired number of average platelets through the thickness is reached, subject to some constraints. The output of the algorithm is an array of discrete representative laminate volume elements (RLVE) with individuated laminate stacking sequences and thicknesses, which may then be utilized to conduct a finite element analysis in Abaqus/Standard [49] or Abaqus/Explicit, depending on the type of results needed. In this work, Abaqus/Standard was used to calculate the elastic properties. The algorithm is the work of Seunghyun Ko and more detail may be obtained from Ko et al. [32]. The general flow of the algorithm is presented in figure 4.1.

4.2.2 Input parameters

The algorithm takes as inputs the geometry of the platelet (length, width, thickness) and the specimen (length, width, thickness), the count and arrangement of specimens to be cut from a single laminate, the target fiber orientation state as defined by the a_{11} term of a 2nd-order orientation tensor, and the side length of the square RLVE. Additional parameters include the tolerance for optimization of the output fiber orientation state as measured by the a_{11} term of the output specimens, and the cutoff threshold for how many optimizations should be attempted at a maximum. Not utilized by this study but a key feature of the algorithm is the ability to specify regional fiber orientation states and so more accurately recreate the complex mesostructure of experimental specimens which have been observed to have significant local variation of the fiber orientation state even within nominally quasi-isotropic specimens.

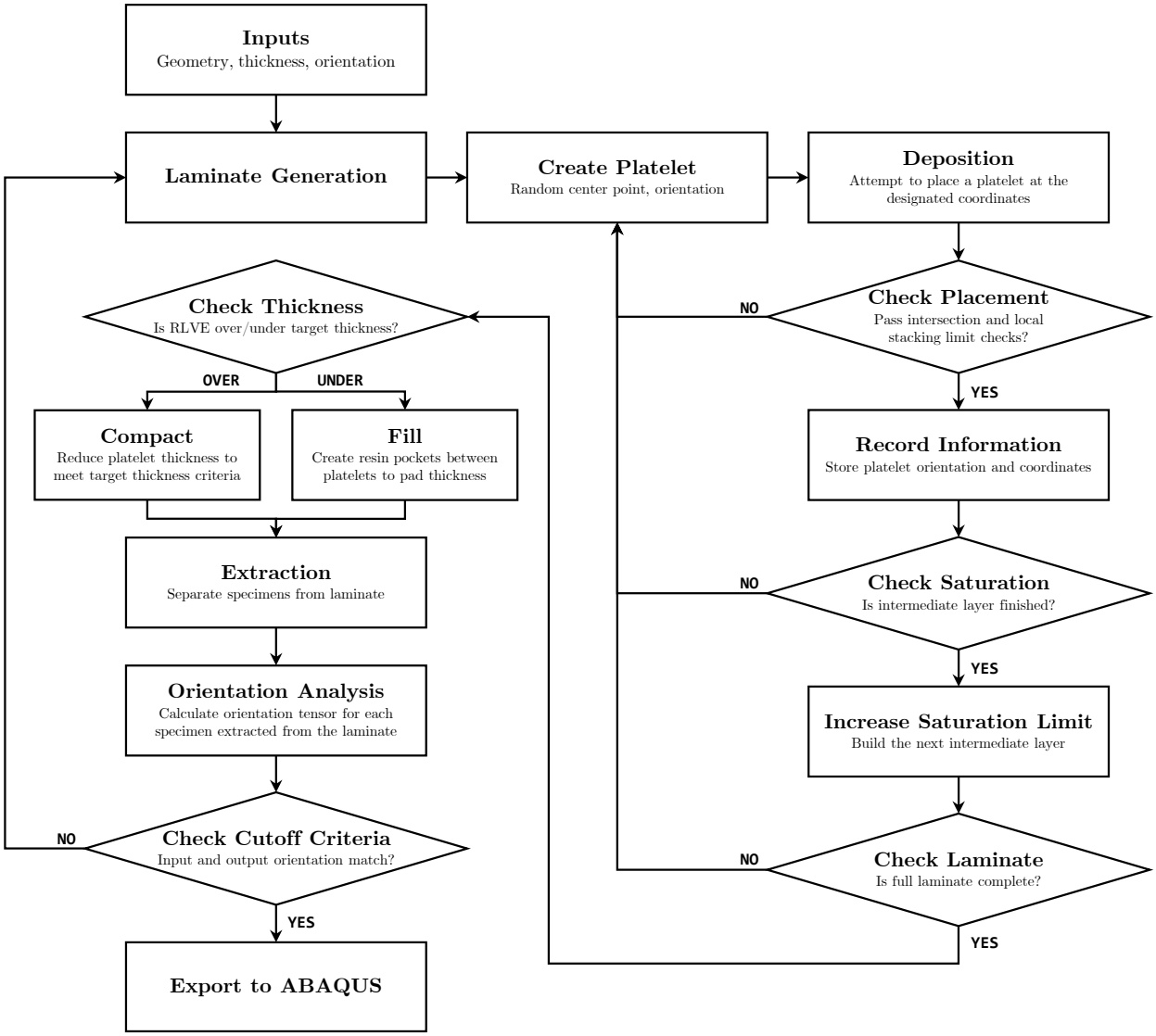

Figure 4.1: Flowchart of the mesostructure generation algorithm

See Ko et al. [32] for additional discussion on the development of the algorithm

4.2.3 Laminate Generation

Laminate generation is the overarching loop that encapsulates the majority of execution time. This step generates a simulated DFC laminate by means of depositing randomly oriented and randomly placed platelets. The geometry of the laminate is determined by the geometry of the specimens and their tiled arrangement. For example, in this work six (6) specimens were tiled width-to-width to form 6" × 6" square panels. To minimize edge effects, the laminate length and width are expanded by 0.5" to create a margin along the edges that will be discarded during specimen extraction. The process is designed to simulate the manufacturing process and specimen preparation steps detailed in sections 2.1.2 and 2.1.3. The laminate is subdivided into a 2D array of RLVEs that contain the through-the-thickness information pertaining to platelet thickness and orientation, and the IDs of the platelets that occupy a given RLVE.

Generation is accomplished by subdividing the through-the-thickness direction into discrete layers, and each layer is generated sequentially, bottom up. For example, a 0.15" thick laminate comprises an average though-the-thickness platelet count of 27 (determined through microscopic examination), and so the full laminate is subdivided into e.g. nine (9) layers that define an intermediate target saturation to ensure that platelets are evenly distributed across the entire laminate, through the entire thickness. This avoids local concentrations and local sparsity that would otherwise occur.

The laminate generation loop is parallelized, such that multiple laminates are generated simultaneously, distributed across some or all of the available processor cores. To ensure uniqueness of the orientations derived from the random number generation, MATLAB's `RandStream` function is used with a Multiplicative lagged Fibonacci generator capable of supporting multiple independent streams and substreams, and each worker thread is assigned a unique substream. This ensures that laminate generation and optimization is entirely independent across processor cores, generation runs, and MATLAB instances.

Typical runtime is approximately 2-3 minutes to generate one (1) laminate for six (6) specimens 6" long by 1" wide with a thickness of 0.15". Utilizing optimization for input/output a_{11} terms with 1% tolerance takes on average 3-4 iterations of the laminate generation loop.

4.2.4 Platelet creation and deposition

To generate a laminate, a function to create and deposit a platelet within the bounds of the laminate geometry is called. Platelet coordinates and orientation are randomly generated using a uniform probability distribution (see section 4.2.9 for a more detailed discussion on this assumption). Once the information for a given platelet is created, an intersection check is conducted to determine which RLVEs the platelet occupies. The intersection checking function comprises a majority share of computation time, and to mitigate the computational cost only the local region of the laminate that includes all possible RLVEs that a platelet could occupy are checked.

Once the RLVEs have been determined, the number of platelets that occupy a given RLVE is checked to ensure that the current intermediate target saturation limit is not exceeded. If a platelet fails an intersection check due to an RLVE containing more platelets through-the-thickness than are currently allowed, the platelet is discarded and the process is repeated until either the checks are passed, or a maximum number of failed attempts for an intermediate target saturation limit is reached. For the simulations undertaken in this work, a cutoff threshold of 1000 total failed attempts per intermediate layer was used.

If a platelet is successfully deposited, the information pertaining to its coordinates and orientation are stored in the set RLVEs which the platelet occupies.

4.2.5 Saturation thresholds

The laminate is generated through-the-thickness in layered subdivisions. Each layer, starting with the first, is subject to an intermediate limit on the average number of platelets through-

the-thickness, and the sum total of these layers produces the final target average number of platelets. For example, a target average of 27 platelets through the thickness leads to 9 subdivisions, each layer attempting to attain an average through-the-thickness of 3 platelets. In practice this limit represents an asymptote, and convergence is not achievable over a reasonable time frame, if at all. Utilizing microscopic analysis, the coefficient of variation in the average number of platelets through the thickness of a 0.15" thick specimen was determined, and is used to create headroom in the target average platelet value.

The higher limit created through the application of the microscopically-derived CoV allows for convergence to the target average platelets. When the saturation limit is reached, or the number of failed placement attempts reaches the cutoff threshold, the saturation limit is increased and the next subdivision is filled. This process repeats until the entire laminate has been generated, as determined by reaching the overall target average platelets through-the-thickness specified as an input parameter.

4.2.6 Thickness validation in RLVEs

The application of the CoV to the saturation limits produces the result that, though the target average platelets through-the-thickness is at the desired value, the maximum number of platelets through-the-thickness is greater. Correcting this, so that the geometry of the laminate is as intended, involves a process whereby every RLVE is iterated over and a determination of the number of platelets within an RLVE is made. If the number of platelets is less than the target average, a number of resin layers are randomly inserted between platelets to mimic behavior seen experimentally where platelet-sparse regions have a decreased local fiber volume fraction and increased resin content. If the number of platelets is greater than the target average, the thickness of each platelet is reduced so that the stack is the appropriate thickness in total, replicating behavior where platelet thickness in dense regions is below the initial thickness of the cured prepreg.

4.2.7 Specimen extraction and orientation analysis

The final step in laminate generation is the calculation of the a_{11} terms for the virtual specimens. To do this, first the specimens are extracted from the laminate and stored in separate arrays, mimicking the process in chapter 2 section 2.1.3. The orientations of all the fiber layers within every RLVE is then used to determine the orientation state of the virtual specimen, and the a_{11} term of the 2nd-order orientation tensor is compared with the target a_{11} input parameter. If the two values are within tolerance, the data is saved to disk, and the generation moves to the next a_{11} input parameter, if one exists. If the two values are not within tolerance, the laminate generation routine is repeated and a new laminate is constructed.

4.2.8 Matching input and output orientation tensor terms

Handling of laminate data when the tolerance threshold is not met is not as simple as discarding the information and repeating the generation. Multiple generation cycles are often necessary in order to generate a laminate that satisfies the target fiber orientation state. While this process unfolds, the laminate with an output a_{11} that is the closest match to the target a_{11} is stored in RAM. If a laminate is generated that is a better match than the laminate in storage, but that does not meet the tolerance threshold, the laminate in memory is replaced with the better matching laminate. If the cutoff threshold for generation attempts is reached before a laminate has been generated that meets the tolerance threshold, the closet match is saved to disk. Often this match will have an a_{11} that is within 1-2% of the target value, just slightly outside tolerance.

Additionally, using a bisection optimization method the a_{11} input parameter may be adjusted to attempt to drive the a_{11} output value towards the target value. The target value is not modified in any way. Given the high variability in the randomly generated mesostructure, the influence of this operation is slight as compared with omitting this process entirely. It

has been observed that convergence in some instances may consistently be reached more quickly, or at all, with this optimization routine enabled than if it is disabled for particular sets of input parameters. The opposite has also been observed. As the goal with this entire process is the generation of a laminate that meets the target criteria as quickly as possible, the engagement of the optimization routine is optional.

4.2.9 The assumption of uniformity

The main assumption of the mesostructure generation algorithm is that a uniform probability distribution, suitably bounded, may sufficiently approximate the real-world, non-uniform fiber orientation distribution for a given fiber orientation state. There has historically been good agreement between simulation and experiment (see Ko et al. [32, 29]) over low-flow regions where a uniform probability distribution is the real-world probability distribution, but over the regions of interest in this work the limitations of this assumption have become clearer, as will be shown in chapter 5. A key limitation of this approach are that orientations along the transverse direction are cut off for specimens with highly-aligned longitudinal orientations, and vice versa. Advani and Tucker [42] and Chen et al. [48] describe methodologies to recover an approximation of the fiber orientation probability density function ψ from a 2nd-order orientation tensor, and Breuer et al. [50] evaluate a number of these approaches for accuracy and reliability, which will be discussed in more detail in section 4.5.

In order to return the complete range of possible a_{11} values through the use of uniform probability distributions, boundary conditions that denote the upper and lower limits on the uniform probability distribution needed to be determined, tied to a given a_{11} input parameter. The boundary conditions were determined numerically by solving equation 4.1 for B_l with $a_{11} \in [0, 0.5)$ and setting $B_u = \pi/2$, and then solving for B_u with $a_{11} \in [0.5, 1]$ and setting $B_l = 0$.

$$a_{11} = \frac{1}{B_u - B_l} \int_{B_l}^{B_u} \cos^2(\theta) d\theta \tag{4.1}$$

Figure 4.2 provides the results of the numerical solver, in the original constraints for $\theta \in [0, 90]$, which was expanded by symmetry to encompass $\theta \in [0, 180]$ for $a_{11} \leq 0.5$, and $\theta \in [-90, 90]$ for $a_{11} \geq 0.5$, to simplify usage of the uniform random number generator in MATLAB. For use with the algorithm, 3601 discrete boundary limits were calculated, indexed by a_{11}, and the algorithm refers to the closest match when selecting the constrained distribution that should produce the desired output a_{11}.

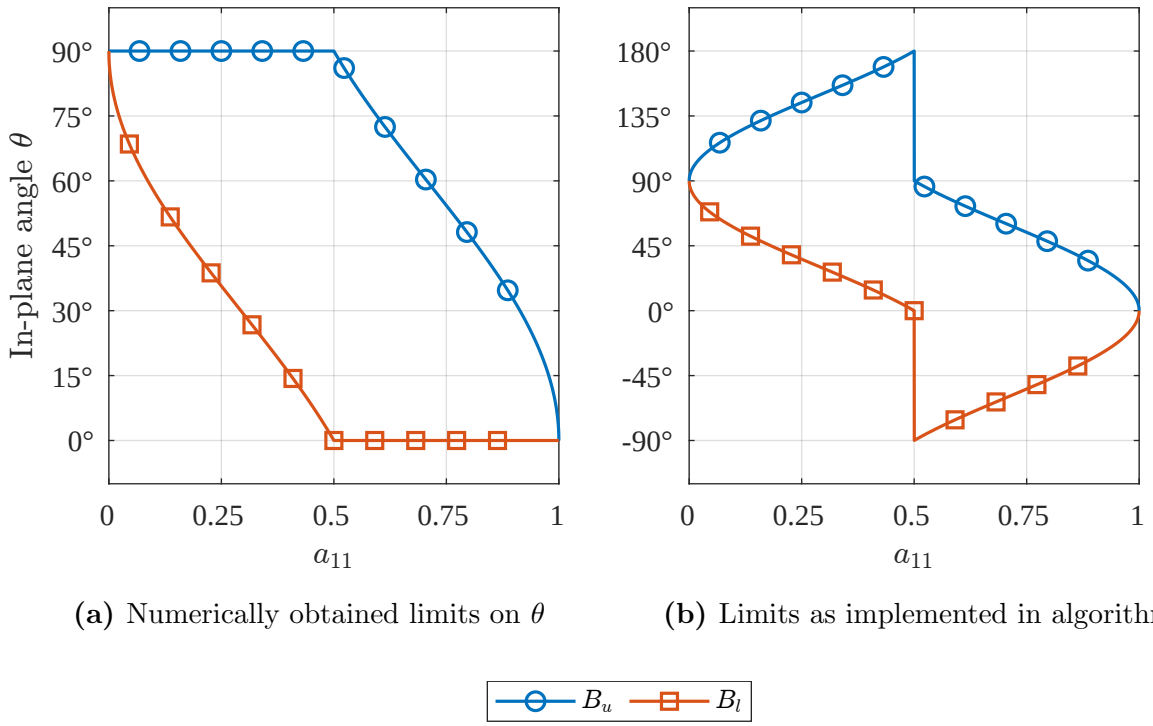

(a) Numerically obtained limits on θ **(b)** Limits as implemented in algorithm

Figure 4.2: Boundary conditions for use with a uniform probability distribution

4.3 Finite Element Analysis

4.3.1 Abaqus/Standard input file

An Abaqus input file is written in MATLAB, converting the geometry, orientations, and thicknesses within the RLVEs output from the mesostructure generation algorithm into a format usable by Abaqus. The general structure of the file is a series of parts containing nodes and elements with orientations and thicknesses assigned by distribution tables. Each part is a single layer of the array of RLVEs, with a 0.15" thick specimen typically having 33 layers. Within parts, two (2) sections are used to group the resin elements and fiber elements and assign material properties. Parts are instanced within an assembly, and boundary conditions, loading, and reporting parameters are set.

Writing of the input file takes approximately 2-3 seconds for a typical virtual specimen, and is parallelized. Pre-processing during simulation takes 2-3 minutes in Abaqus/Standard, with a typical simulation running 8-9 minutes. For this work, simulations were run in parallel, 8 at a time.

4.3.2 Simulation parameters

Preparation of a virtual specimen entails the definition of the type of finite elements to use, and assignment of boundary conditions and loadings to nodes and elements. For this work, S4R shell elements were used (figure 4.3a) which are commonly employed for composite simulations. The primary feature is that a 3D shape may be reduced to a 2D finite element when the thickness is significantly smaller than the length or width. Elements were sized to match the RLVEs output by the mesostructure generation algorithm, 5 mm $\times$ 5 mm. Thickness of each element was specified based on the thickness information contained for each layer within the RLVEs.

The specimens were assigned boundary conditions and loadings consistent with figure

4.3b. A reference point was created at the center of the top and bottom faces, and all nodes comprising the top and bottom surfaces connected to those reference points with a rigid body constraint. The bottom reference point was constrained in rotation and displacement, and the top point constrained in rotation and displacement, except for translation along the loading direction. A traction load was applied to the top reference point to simulate the tensile tests. The node sets comprising the ply layers were tied to each other in sequence, with the top face of the bottom layer tied to the bottom face of the second layer, with the top surface of the second layer tied to the bottom layer of the third layer, and so on.

(a) S4R Shell Element **(b)** Loading and boundary conditions

Figure 4.3: Shell elements, loading and boundary conditions used with FEA

A static analysis was conducted with an initial time increment and time period of the step of 1. The minimum time increment was set to 1×10^{-12}, with a maximum time increment of 1. The step was configured to perform a geometrically linear analysis. The simulation outputs

the reaction force and displacement at the top reference point, allowing for the calculation of the elastic modulus based on the stress and strain measured during the simulation and the geometry of the specimen.

The results of the simulations were extracted from the output database files using Python.

4.4 Optimizations

The parameter sweep required for this work necessitated significant optimizations to the existing mesostructure generation algorithm and the related Abaqus input file writer in order for the required number of simulations to be achievable within a reasonable time span. Optimizations to the mesostructure generation algorithm and the Abaqus input file writer are detailed in this section.

4.4.1 Improvements to the Mesostructure generation algorithm

As initially configured, generation of a 0.15" thick laminate with 6 specimens, nominally 7" × 7" square, required 11-12 minutes, and the process was not parallelized, or even parallelizable as written. In this condition, with optimization of a single laminate taking between 1-2 hours on average, generation of the 707 laminates used in this work would have required between 30-60 days of continuous generation.

Significant profiling of the mesostructure generation algorithm was performed to identify bottlenecks and apply optimizations. Extensive vectorization of `for` loops and elimination of the use of `cell` data types and `cellfun` realized significant performance gains. Conversion of the use of `rand` to a customized version of `unifrnd` that supports `RandStream` saw significant improvements to platelet creation and deposition. Further performance gains were realized by optimization of the intersection checks used to determine which RLVEs were occupied by a platelet in process of being deposited. Previously the whole laminate was checked, but by reducing this to a subset that comprises the set of possibly occupied RLVEs only, the

performance of the intersection check was substantially improved.

Saving to disk is a time consuming process that had been performed with every laminate generation. As laminate generation includes an optimization routine, these files were written and overwritten multiple times. The process was revised to store the laminate with a fiber orientation state closest to the target output in memory, until either optimization was achieved or the cutoff point met. Writing to disk thus occurs only after all generation is completed.

Once the optimization of the laminate generation loop was completed to the extent feasible, parallel processing was implemented using MATLAB's `parfor` routine to encapsulate the laminate generation and optimization routines. In order to resolve an issue with the MATLAB random number generator, where random number streams are not unique between MATLAB instances and `parpool` instances, `RandStream` was implemented as described in section 4.2.3 to support multiple independent, unique random number streams. Seeds were shuffled with each run of the algorithm to avoid non-unique seeds between runs.

The performance gains thus employed realized a net reduction in computation time up to 4×-6× in the main laminate generation and optimization loop over the original state of the algorithm. With parallelization, on a workstation with an Intel i9 12-core processor, overall performance gains were between 48×-60× faster, allowing for complete generation of a fiber orientation sweep in a matter of hours, and full generation of all 4,242 specimens in less than two days.

4.4.2 Improvements to the Abaqus input file generator

The greatest performance gains were realized with a complete overhaul of the Abaqus input file writer, which was written in MATLAB. The Abaqus input file writer formerly depended on assigning each element to a section in order to assign unique orientation, thickness, and material properties. As originally written, a typical input file for a 0.15" thick specimen would

generate with over 500,000 sections, which would result in a lengthy pre-processing step that took over 30 minutes. Simulations were reasonably performant, requiring 12 minutes for a typical 0.15" thick specimen. However, post-processing required 40+ minutes to even open the output database file for reading. Even writing the input file to disk required several minutes. In this condition, simulation of the 4,242 specimens evaluated in this work would have required more than 250 days of continuous simulation.

The most important optimization involved first the reworking of the internals to utilize distribution tables, and second to exploit vectorization of `fprintf` and `for` loops wherever possible. This reduced the number of sections to 66 for a typical 0.15" thick specimen with 33 ply layers, and reduced the size of the input file by a factor of 3. Writing the input file to disk was reduced to 1-2 seconds, and the Abaqus input file writer was adjusted to take advantage of MATLAB's parallelization features.

The net performance gains realized from these optimizations was a 10×-15× faster pre-processing step, completing in 2-3 minutes on average. Simulations completed 1.5× faster, and most significantly, post-processing went from more than 40 minutes to 1-2 seconds, a reduction by a factor of more than 1600. Overall, simulations, including pre-and-post-processing, were reduced from nearly 1.5 hours to an average of 10 minutes, with an associated reduction in the memory footprint that enabled the simultaneous execution of 8 simulations in parallel on a workstation with 128 GB of memory. Simulation of all 4,242 specimens required less than four days.

4.5 Future work

The investigation into the effects of platelet morphology and flow condition are in part intended to facilitate the improvement and extend the development of the in-house simulation tools.

4.5.1 Implementation of non-uniform fiber orientation distributions

Advani and Tucker [42] proposed the use of even-ordered orientation tensors as a means to recover the fiber orientation distributions through a reconstruction of the probability density function ψ. The methodology involves the use of progressively higher-order orientation tensors, but the infinite series may be truncated. The authors found that the use of a 2nd and 4th-order orientation tensor were sufficient to approximate the fiber orientation distribution of a short-fiber composite, and further proposed a hybrid closure approximation to calculate the 4th-order orientation tensors from a 2nd-order orientation tensor using linear and quadratic closure approximations. This methodology has been implemented widely in industry in the field of short-fiber composite modelling in Abaqus, Autodesk Moldfow and others [51, 52].

Breuer et al. [50] in 2019 conducted an extensive evaluation of the accuracy of these reconstruction methodologies, as it has been noted that a 2nd-order orientation tensor is an ambiguous description of an orientation density function, and is non-unique. It was found that the quality of the reconstruction depends significantly on the original fiber orientation being reconstructed [50]. As these methods were originally developed for composites with short fibers embedded in a matrix solution for use with injection molding, which can induce significant variability in fiber orientations, the comparatively more regular features of discontinuous fiber composites may be more suitable to these methodologies.

Chen et al. [48] presented an approach using a Gauss error function to recover probability density functions from simulated fiber orientation distributions, and as shown in this work

the resulting PDFs have good agreement with the experimentally observed probability distributions. In order to improve the in-house mesostructure generation algorithm, and replace the assumption of a uniform probability distribution, the Gauss error function is presently being integrated into the mesostructure generation algorithm, and further simulations will be conducted to see how the elastic properties of specimens created using the non-uniform probability distributions compare with those created using the uniform probability distributions, and whether features seen in chapter 5 appear or not.

Chapter 5
SIMULATION RESULTS AND ANALYSIS

Analysis of the elastic properties of narrow and square platelets determined from finite element analysis are presented in this chapter. The elastic moduli are presented in terms of the fiber orientation state as represented by the a_{11} term of a 2nd-order orientation tensor, which was calculated for each of the virtual specimens. As out-of-plane effects were neglected for these simulations $a_{33} = 0$, and the a_{22} term is therefore simply $a_{22} = 1 - a_{11}$, and the simplification to use only the a_{11} term is justified.

5.1 Elastic properties

5.1.1 General observations

Inflection in simulations of elastic modulus near $a_{11} = 0.5$

Examination of the simulation sweeps in figures 5.1 and 5.2 reveal that there exists an inflection point at $a_{11} = 0.5$ in the trends of the elastic moduli. It is speculated that this relates to the imposition of uniform probability distributions, as the boundary conditions similarly have inflections at that point (see figure 4.2). The shape of the sweeps may not reflect the physical reality, despite general agreement with the experimental data over the experimental range investigated, and improvements to the model to utilize a more realistic, non-uniform probability density function in place of a uniform probability density function are in progress.

Scatter in the simulation data

It is observed that the simulations using the narrow platelet geometry have low scatter along the axis of elastic modulus, on the order of 1%, as seen in figure 5.1. This does not reflect the experimental observations, where very large scattering with standard deviations averaging 10.4% for narrow platelet specimens were observed in the data (see table 3.2 and appendix A). It is notable that the scatter in the simulations using the square platelet geometry, by contrast, are much larger, closer to 5%, and are a better fit for the experimental observations where the average standard deviations for square platelet specimens were 7.4%, as shown in figure 5.2. The scatter is still lower than that seen in the experimental data, but is greater than with the narrow platelet simulations, and closer to the physical reality.

Given that square platelets deposited by the algorithm produce a greater degree of overlap and resin-rich areas than the narrow platelets, greater variability in the fiber volume fraction may account for the larger scatter in elastic modulus observed in the simulations. The narrow platelets by contrast are deposited more densely on account of their narrower width.

Additionally, the model does not capture out-of-plane effects at all. As information available in the literature and the observations of fiber orientation distributions in this work strongly suggest, out-of-plane effects have a significant influence on the elastic modulus of DFC parts and are not negligible in order to capture realistic scatter in material properties. Capturing those effects is complicated, and improvements to the model to better explore these effects in simulation are in progress. Several research groups are presently engaged in the development of models that accurately and comprehensively capture these complexities [29, 32, 34, 37, 48].

5.1.2 Sweep of fiber orientations for narrow platelets

Simulations for three (3) thicknesses, 0.065", 0.15" and 0.25", using virtual specimens generated using narrow platelets were conducted using finite element analysis to determine the

elastic behavior. 606 simulations were conducted for 0.065" and 0.25" thick specimens, and 1212 simulations were conducted for 0.15" thick specimens, sweeping through the fiber orientation state determined by the a_{11} input parameter. The discrepancy arises from the fact that 0.15" thick specimens were simulated first, after which it was observed that the scatter in the data was not large, and 12 simulations for each discrete a_{11} input parameter was unnecessary.

Results of these simulations are presented, overlaid with the experimental results, in figure 5.1. It is observed that there is good agreement (within 2%) between the simulations and the experimental results for the high-flow condition, as seen in 5.1c. There is similarly good agreement (within 2%) between the experimental results and the simulations for 0.15" and 0.25" thick specimens. However, the simulations for the 0.065" thick specimens significantly underpredict the elastic moduli seen in the experimental data by nearly 20%. It is unclear where this discrepancy arises, but it is speculated that difficulties in reaching the saturation limits for very thin specimens with the mesostructure generation algorithm is related. It is noted that the coefficient of variation term that determines the bounds of the saturation limits within the mesostructure generation algorithm were determined from microscopy of the 0.15" thick specimens and the values may be different for the 0.065" thick specimens. Likewise, as mentioned in section 3.2.1, the very thin specimens are outside the limits recommended by the manufacturer. Additionally, the more complex mesostructure features such as porosity, waviness and out-of-plane orientations are not captured by the model.

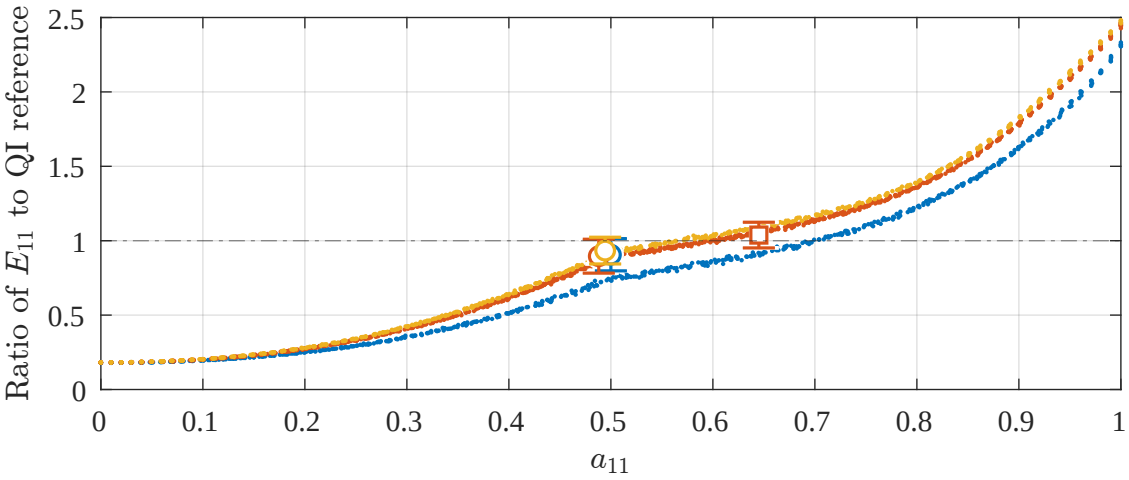

(a) Complete sweep of in-plane fiber orientations

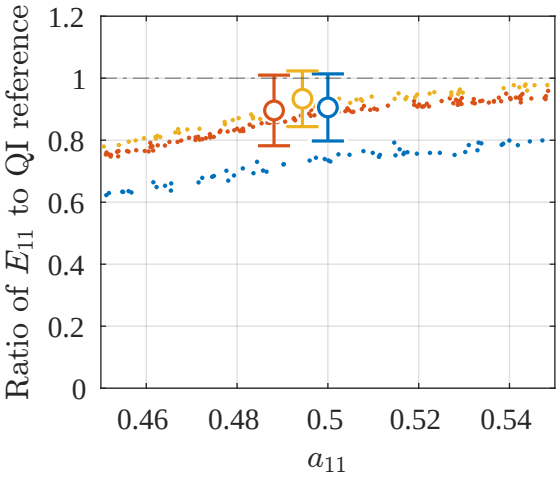

(b) Low-flow close-up

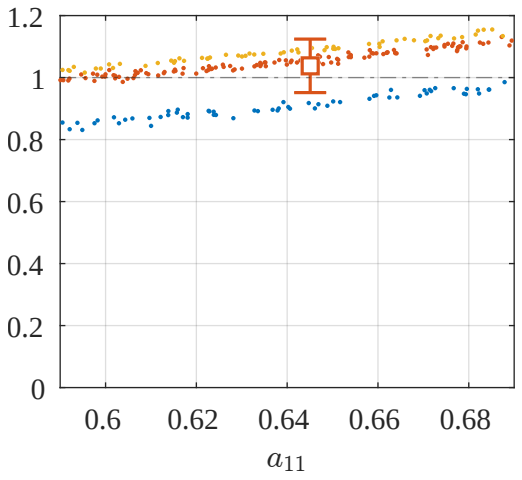

(c) High-flow close-up

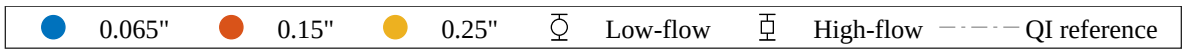

Bars represent one standard deviation from the mean

Figure 5.1: Simulated sweep of fiber orientation states for narrow platelet specimens. Dots represent simulations, symbols with bars represent experiments

5.1.3 Sweep of fiber orientations for square platelets

Simulations for three (3) thicknesses, 0.065", 0.15" and 0.25", using virtual specimens generated using square platelets were conducted using finite element analysis to determine the elastic behavior. 606 simulations were conducted for each thickness, sweeping through the fiber orientation state determined by the a_{11} input parameter. Results of these simulations are presented, overlaid with the experimental results, in figure 5.2. Experimental data for 0.25" thick specimens manufactured with square platelets are not presently available for comparison with simulation, but it is planned to conduct those experiments in the future to expand the available data set.

It is observed that there is good agreement (within 2%) between the simulations and the experimental results for the high-flow condition, as seen in 5.2c. As a contrast to the narrow platelet simulations above, here the simulations for 0.065" thick specimens have good agreement (within 2%) with the low-flow experimental results as shown in figure 5.2b. However, the simulations for the 0.15" thick specimens underpredict the elastic moduli as compared with the experimental results by nearly 10%. Additionally unlike in the experimental results, where it was found that square platelet specimens in general have an elastic modulus nearly 10% lower than the narrow platelet specimens, here in the simulated sweeps comparable narrow and square platelet specimens have a nearly identical elastic modulus. This is attributed to the simplistic nature of the generated mesostructure compared to the more complicated reality, as porosity and out-of-plane characteristics are not captured.

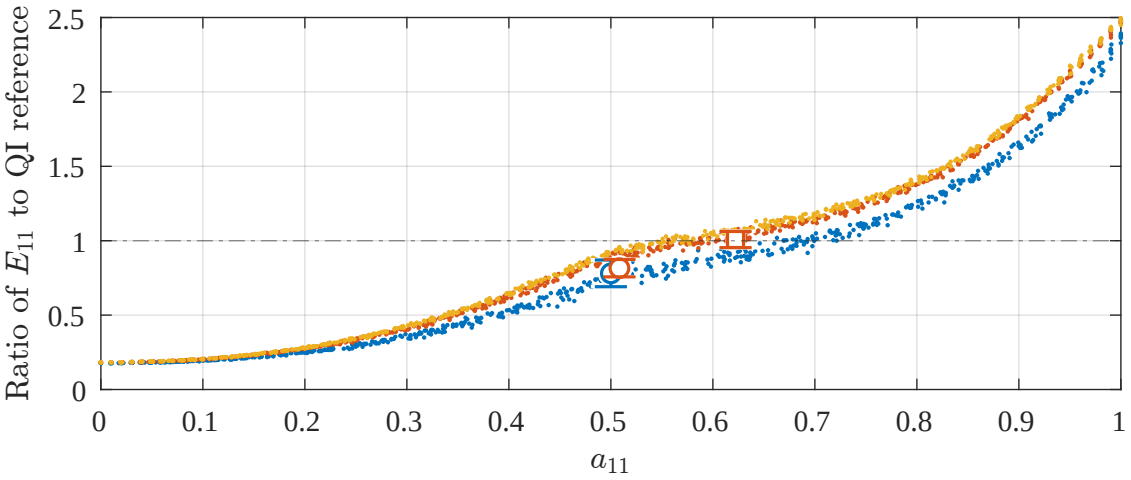

(a) Complete sweep of in-plane fiber orientations

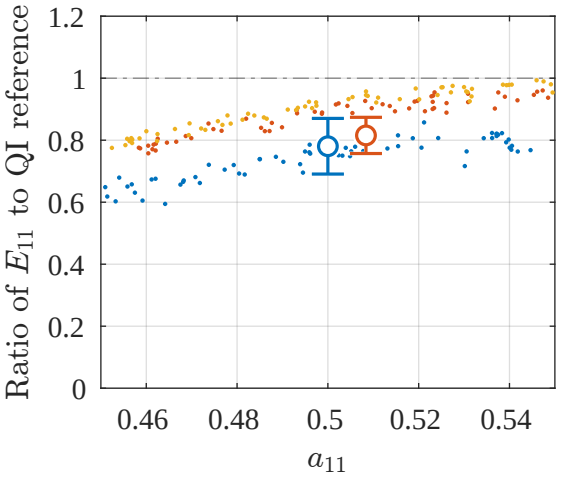

(b) Low-flow close-up

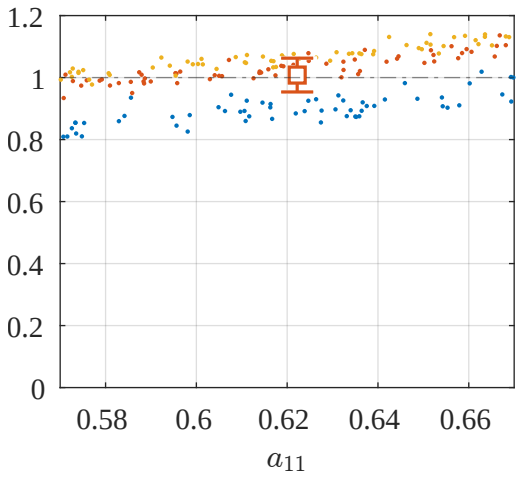

(c) High-flow close-up

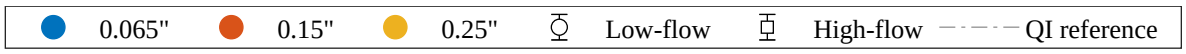

Bars represent one standard deviation from the mean

Figure 5.2: Simulated sweep of fiber orientation states for square platelet specimens. Dots represent simulations, symbols with bars represent experiments

Chapter 6
CONCLUSION

The aim of this work was to investigate and characterize the effects of platelet morphology and flow conditions on the elastic properties and fiber orientation states of discontinuous fiber composite structures. Physical tensile testing combined with microcomputed tomography and micrography were employed to produce an experimental baseline and characterize the mesostructure. A virtual study of the full range of in-plane fiber orientation states was conducted using an in-house mesostructure generation algorithm and finite element analysis simulations.

The elastic properties were found to be strongly influenced by the manufacturing-induced flow conditions, and moderated by the platelet morphology. In low-flow conditions, where a minimum amount of lateral displacement occurs, the elastic modulus of discontinuous fiber composites were consistently an average relative difference of 13.3% lower than a quasi-isotropic (QI) continuous fiber composite reference. An average relative difference of 9.2% and 22.5% from the QI reference was observed for narrow platelet and square platelet specimens respectively, indicating that platelet morphology moderates this reduction. Conversely for high-flow conditions, the elastic modulus exceeds that of the QI reference by a relative difference of 2.9% on average, with platelet morphology leading to an increase of 3.7% and 0.8% for narrow platelet and square platelet specimens, respectively. It was observed that square platelet specimens consistently underperform narrow platelet specimens, moderating the trends observed for flow conditions. However, scatter within the elastic properties responds primarily to platelet morphology, with square platelets having lower standard deviations than narrow platelets by an average of 41.6% for low-flow conditions, and 44.0% for

high-flow conditions.

Fiber orientation state was found to strongly depend on the flow conditions, with platelet morphology having only a small influence. Evaluation of the 2nd-order orientation tensors found a 52% relative increase in the in-plane longitudinal alignment from low-flow to high-flow conditions. In low-flow conditions, the in-plane fiber orientation distributions are very nearly uniform, with square platelets only slightly more evenly distributed than narrow platelets in the plane. High-flow conditions in-plane are moderately more responsive to platelet morphology, with narrow platelets being more prone to aligning with the flow direction than square platelets by a relative difference of 8.3%. A similarly large relative increase of 54.5% was observed in the out-of-plane alignment of the orientation tensors from low-flow to high-flow. Out-of-plane orientations in low-flow conditions responded more to platelet morphology, with square platelets being 28% less likely to align out-of-plane than narrow platelets. This effect disappears entirely at high-flow, where flow conditions dominates platelet morphology completely, with a 1.8% relative difference observed in the peaks of the out-of-plane distributions that are otherwise virtually identical.

A qualitative analysis of the mesostructure of discontinuous fiber composites using micrography found flow condition to have significant impacts. Micrographs of the narrow platelet specimens in low-flow conditions were observed to have clear, distinct platelet boundaries with consistent thickness, and a minimum of resin pockets. High-flow conditions by contrast induced significant turbulence and increased waviness in the platelets. Platelet boundaries were observed to be indistinct with substantial mixing of the fibers, and the presence of voids not seen in the low-flow condition were found throughout the samples.

A virtual study using an in-house mesostructure generation algorithm was found to have good agreement, within 2% of the experimental data, over the range of experimentally investigated fiber orientation states. However, the scatter observed in the simulations was below that observed in the experiments, with simulated narrow platelet specimens having standard

deviations on the order of 1% compared with the 10.4% observed in experiments. Simulations of square platelet specimens performed better in this regard, with standard deviations on the order of 5% compared with the 7.4% observed in experiments. The limitations of the assumption of bounded uniform probability distributions were observed, and based on the comparison of empirically determined fiber orientation distributions to the work of Chen et al. [48] in simulating a non-uniform probability distribution, a Gauss error function will replace the uniform probability distributions within the mesostructure generation algorithm in the future.

In summary, elastic properties and fiber orientation state are strongly dependent on the manufacturing-induced flow conditions. Platelet morphology strongly influences the scatter in material properties, and modulates the effect of flow conditions on the elastic properties and fiber orientation states. The virtual study showed good agreement over the experimentally investigated range of fiber orientation states, but the use of bounded uniform probability distributions to control fiber orientation states is a limiting factor. A non-uniform Gauss error function proposed by Chen et al. as a means to numerically approximate the probability density functions of fiber orientation states was shown in this work to match with experimentally observed fiber orientation distributions, and will replace the uniform probability distributions in the in-house mesostructure generation algorithm.

REFERENCES

[1] Bowen, J., "From Cirium's chief executive officer," *The Cirium Airline Inisghts Review 2020*, 2020, pp. 5–7.

[2] Mazareanu, E., "Revenue of commercial airlines worldwide from 2003 to 2021," `https://www.statista.com/statistics/278372/revenue-of-commercial-airlines-worldwide`, Accessed: May 10, 2021.

[3] Gubisch, M., "Airlines go big on early retirements," *The Cirium Airline Inisghts Review 2020*, 2020, pp. 45–46.

[4] Doyle, A., "Greener on the other side," *The Cirium Airline Inisghts Review 2020*, 2020, pp. 49–50.

[5] Mazareanu, E., "U.S. airline fuel cost from 2004 to 2020," `https://www.statista.com/statistics/197689/us-airline-fuel-cost-since-2004`, Accessed: May 10, 2021.

[6] Mazareanu, E., "Total fuel consumption of commercial airlines worldwide between 2005 and 2021," `https://www.statista.com/statistics/655057/fuel-consumption-of-airlines-worldwide`, Accessed: May 10, 2021.

[7] The Boeing Company, "Commercial Market Outlook 2019-2038," Sep. 2019.

[8] The Boeing Company, "Commercial Market Outlook 2020-2039," Oct. 2020.

[9] Daniel, I. M., *Engineering mechanics of composite materials*, Oxford University Press, New York, second edition. ed., 2006.

[10] Unndorsonn, R., Jonsson, M. P., and Runarsson, T., "NDT Methods for Evaluating Carbon Fibre Composites," *Comptest*, 2004.

[11] The Boeing Company, "Boeing: 787 By Design," `https://www.boeing.com/commercial/787/by-design`, Accessed: May 10, 2021.

[12] Averill, B., "Modern Materials," https://chem.libretexts.org/@go/page/349657, 9 2021, Accessed: Jan. 30, 2020.

[13] Terdiman, D., "In Wichita, the 787 Dreamliner gets its head start," https://www.cnet.com/news/in-wichita-the-787-dreamliner-gets-its-head-start/, Accessed: May 18, 2021.

[14] Johnson, T., "Thermoplastic vs. Thermoset Resins," https://www.thoughtco.com/thermoplastic-vs-thermoset-resins-820405, Accessed: May 18, 2021.

[15] King, J., "Failure in composite materials," *Metals and Materials*, Vol. 5, No. 12, December 1989, pp. 720–726, This is an Accepted Manuscript of an article published by Taylor & Francis in Metals and Materials in December 1989.

[16] Hale, J., "Boeing 787 from the Ground Up," *AERO*, Vol. 24, No. 4, 2006, pp. 17–23.

[17] Marsh, G., "Boeing's 787: trials, tribulations, and restoring the dream," *Reinforced Plastics*, Vol. 53, No. 8, 2009, pp. 16–21.

[18] NORDAM, "NORDAM Makes 20,000th Composite Window Frame For Boeing 787," http://nordam.com/news/nordam-makes-20000th-composite-window-frame-boeing-787, Accessed: Jan. 22, 2020.

[19] Boursier, B. and Lopez, A., "Failure initiation and effect of defects in structural discontinuous fiber composites," *International SAMPE Technical Conference*, 2010.

[20] Johnson, T., "Composites in Aerospace," https://www.thoughtco.com/composites-in-aerospace-820418, Accessed: Jan. 23, 2020.

[21] Allvac, "Titanium Ti-6Al-4V (Grade 5), STA," http://www.matweb.com/search/datasheet.aspx?MatGUID=b350a789eda946c6b86a3e4d3c577b39, Accessed: May 17, 2021.

[22] Aluminum Association, Inc., "Aluminum 6061-T6; 6061-T651," http://www.matweb.com/search/datasheet.aspx?MatGUID=b8d536e0b9b54bd7b69e4124d8f1d20a, Accessed: May 17, 2021.

[23] Toray Composite Materials America, Inc., *TORAYCA®Technical Manual*, April 2020.

[24] Toray Composite Materials America, Inc., *2510 Prepreg System*, July 2020.

[25] Toray Composite Materials America, Inc., *3900 Prepreg System*, July 2020.

[26] Arce, M., *Certification of Discontinuous Composite Material Forms for Aircraft Structures*, Master's thesis, University of Washington, 2015.

[27] Markforged, "The Digital Forge," `https://markforged.com/digital-forge`, Accessed: Mar. 16, 2022.

[28] Markforged, "Onyx^{TM}: Micro carbon fiber filled nylon that forms the foundation of Markforged composite parts," `https://markforged.com/materials/plastics/onyx`, Accessed: Mar. 16, 2022.

[29] Ko, S., Davey, J., Douglass, S., Yang, J., Tuttle, M. E., and Salviato, M., "Effect of the thickness on the fracturing behavior of discontinuous fiber composite structures," *Composites Part A: Applied Science and Manufacturing*, Vol. 125, 2019, pp. 105520.

[30] Hexcel, "As Boeing delivers the First 787 Dreamliner, Hexcel Reveals Some of Its Composite Innovations for the Aircraft," `https://www.hexcel.com/News/News-Releases/921/as-boeing-delivers-the-first-787-dreamliner-hexcel-reveals-some-of-its-composite`, September 2011, Accessed: Mar. 16, 2022.

[31] TenCate, "Compression Molded Parts Product Selection Guide," Accessed: Jan. 20, 2021.

[32] Ko, S., Yang, J., Tuttle, M. E., and Salviato, M., "Effect of the platelet size on the fracturing behavior and size effect of discontinuous fiber composite structures," *Composite Structures*, Vol. 227, 2019, pp. 111245.

[33] Feraboli, P., Peitso, E., Deleo, F., Cleveland, T., and Stickler, P. B., "Characterization of Prepreg-Based Discontinuous Carbon Fiber/Epoxy Systems," *Journal of Reinforced Plastics and Composites*, Vol. 28, No. 10, 2009, pp. 1191–1214.

[34] Selezneva, M., Roy, S., Meldrum, S., Lessard, L., and Yousefpour, A., "Modelling of mechanical properties of randomly oriented strand thermoplastic composites," *Journal of Composite Materials*, Vol. 51, No. 6, 2017, pp. 831–845.

[35] Feraboli, P., Cleveland, T., Stickler, P., and Halpin, J., "Stochastic laminate analogy for simulating the variability in modulus of discontinuous composite materials," *Composites Part A: Applied Science and Manufacturing*, Vol. 41, No. 4, 2010, pp. 557–570.

[36] Alves, M. and Pimenta, S., "The influence of 3D microstructural features on the elastic behaviour of tow-based discontinuous composites," *Composite Structures*, Vol. 251, 2020, pp. 112484.

[37] Sommer, D. E., Kravchenko, S. G., Denos, B. R., Favaloro, A. J., and Pipes, R. B., "Integrative analysis for prediction of process-induced, orientation-dependent tensile properties in a stochastic prepreg platelet molded composite," *Composites Part A: Applied Science and Manufacturing*, Vol. 130, 2020, pp. 105759.

[38] Solvay, "APC (PEKK)/AS4D," `https://www.solvay.com/en/product/apc-pekkas4d`, Accessed: Nov 20, 2021.

[39] Solvay, Composite Materials HQ, 4500 McGinnis Ferry Rd, Alpharetta, GA 30005-3914, USA, *APC (PEKK-FC) Technical Data Sheet*, 10 2017.

[40] ASTM International, West Conshohocken, PA, *ASTM D3039 / D3039M-00, Standard Test Method for Tensile Properties of Polymer Matrix Composite Materials*, 2000.

[41] Tang, H., Chen, Z., Zhou, G., Li, Y., Avery, K., Guo, H., Kang, H., Zeng, D., and Su, X., "Correlation between failure and local material property in chopped carbon fiber chip-reinforced sheet molding compound composites under tensile load," *Polymer Composites*, Vol. 40, No. S2, 2019, pp. E962–E974.

[42] Advani, S. and Tucker, C., "The Use of Tensors to Describe and Predict Fiber Orientation in Short Fiber Composites," *Journal of Rheology*, Vol. 31, No. 8, 1987, pp. 751–784.

[43] MATLAB, *9.7.0 (R2019b)*, The MathWorks Inc., Natick, MA, 2019.

[44] MATLAB, *9.9.0 (R2020b)*, The MathWorks Inc., Natick, MA, 2020.

[45] MATLAB, *9.11.0 (R2021b)*, The MathWorks Inc., Natick, MA, 2021.

[46] GOM Metrology, *2019 Hotfix 8, Rev. 131186, Build 2020-09-10*, The MathWorks Inc., Braunschweig, Germany, 2020.

[47] Nakagawa, T., Ko, S., Slaughter, C., Abdullah, T., Houser, G., and Salviato, M., "Effects of Out Time on the Mechanical and Fracture Properties of Chopped Fiber Composites Made From Repurposed Aerospace Prepreg Scrap and Waste," `https://doi.org/10.48550/arXiv.2112.11591`, 2021.

[48] Chen, Z., Huang, T., Shao, Y., Li, Y., Xu, H., Avery, K., Zeng, D., Chen, W., and Su, X., "Multiscale finite element modeling of sheet molding compound (SMC) composite structure based on stochastic mesostructure reconstruction," *Composite Structures*, Vol. 188, 2018, pp. 25–38.

[49] Abaqus/Standard, *Build 2020-03-06 - 06.50.37 167380*, Dassault Systèmes Simulia Corporation, Johnston, RI, 2021.

[50] Breuer, K., Stommel, M., and Korte, W., "Analysis and Evaluation of Fiber Orientation Reconstruction Methods," *Journal of Composites Science*, Vol. 3, No. 3, 2019.

[51] Dassault Systèmes, "SIMULIA User Assistance 2021: Mean-field homogenization," `https://help.3ds.com/2021/english/dssimulia_established/simacaematrefmap/simamat-c-meanfieldhomogenization.htm?contextscope=all`, Accessed: Mar. 17, 2022.

[52] Autodesk, "Moldflow Insight: Theoretical basis for fiber orientation prediction (Theory)," `https://knowledge.autodesk.com/support/moldflow-insight/learn-explore/caas/CloudHelp/cloudhelp/2016/ENU/MoldflowInsight/files/GUID-50FF496F-0E3E-43CE-B30B-4B12CC24F7DE-htm.html`, Accessed: Mar. 17, 2022.

Appendix A

SCATTERPLOTS OF ELASTIC MODULUS E_{11}

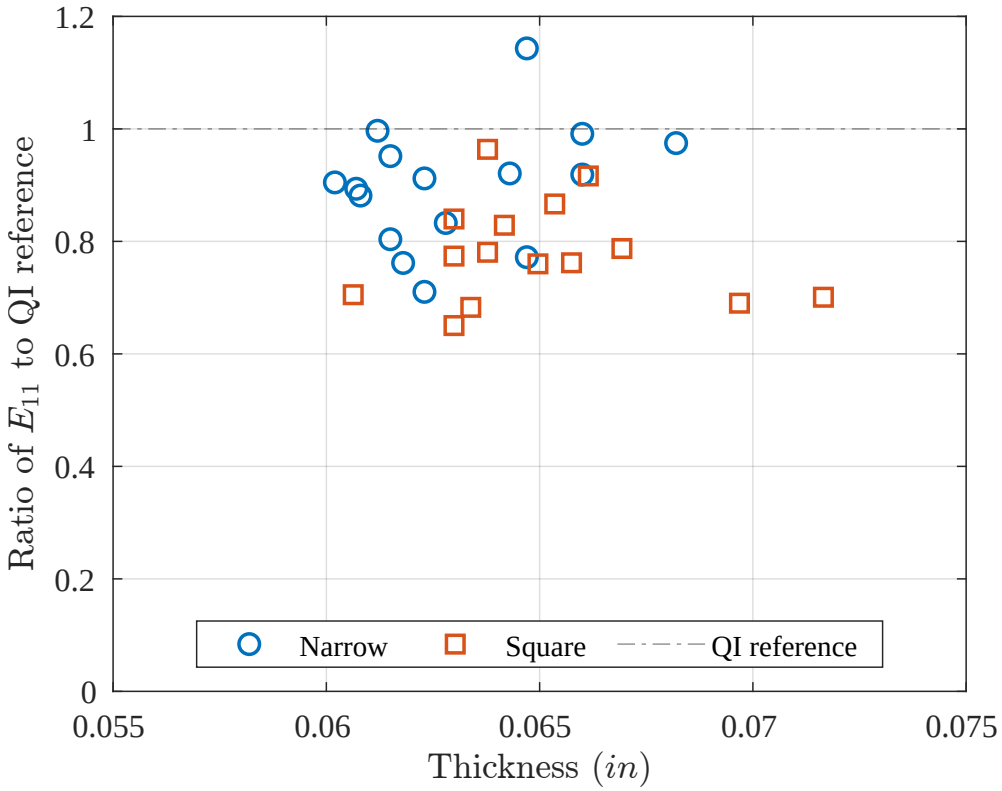

Figure A.1: Low-Flow, Narrow vs Square Platelet:
Scatterplot of E_{11} for nominally 0.065" thick specimens manufactured with narrow or square platelets, using a low-flow process

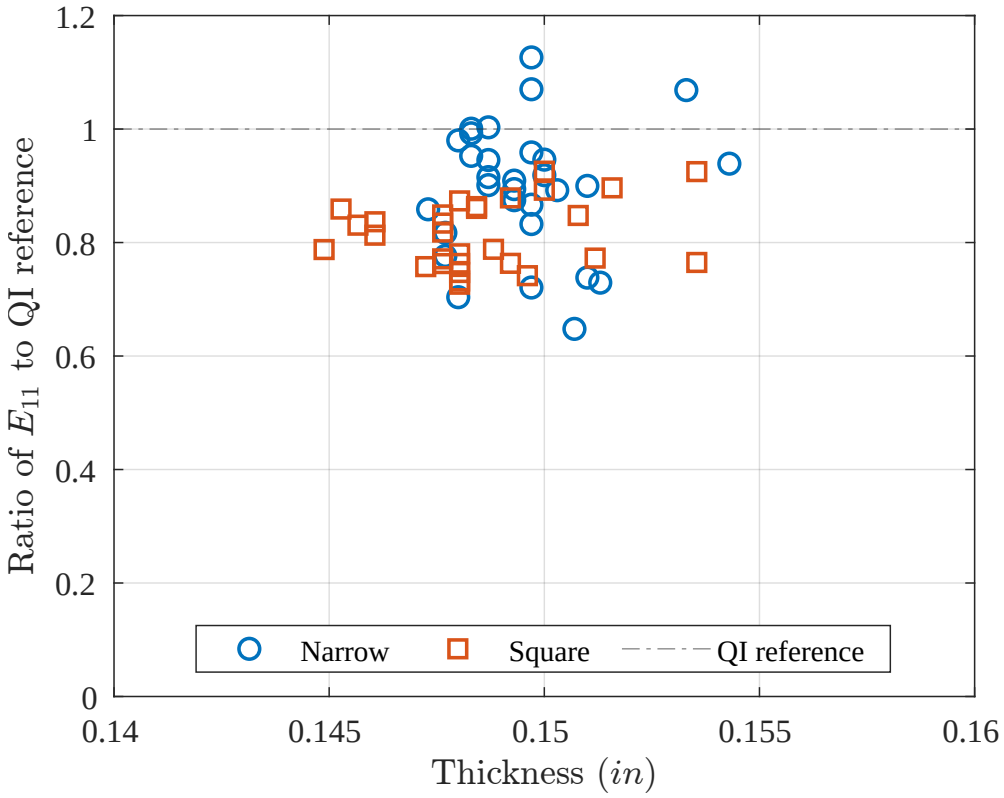

Figure A.2: Low-Flow, Narrow vs Square Platelet:
Scatterplot of E_{11} for nominally 0.15" thick specimens manufactured with narrow or square platelets, using a low-flow process

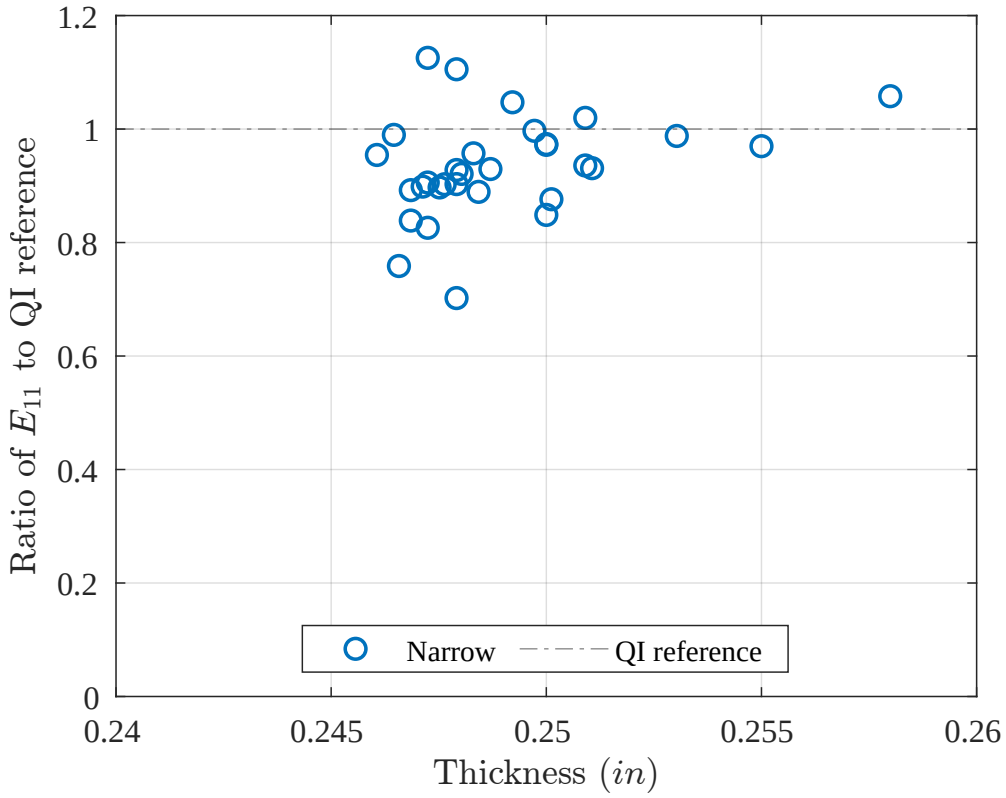

Figure A.3: Low-Flow, Narrow Platelet:
Scatterplot of E_{11} for nominally 0.25" thick specimens manufactured with narrow platelets, using a low-flow process

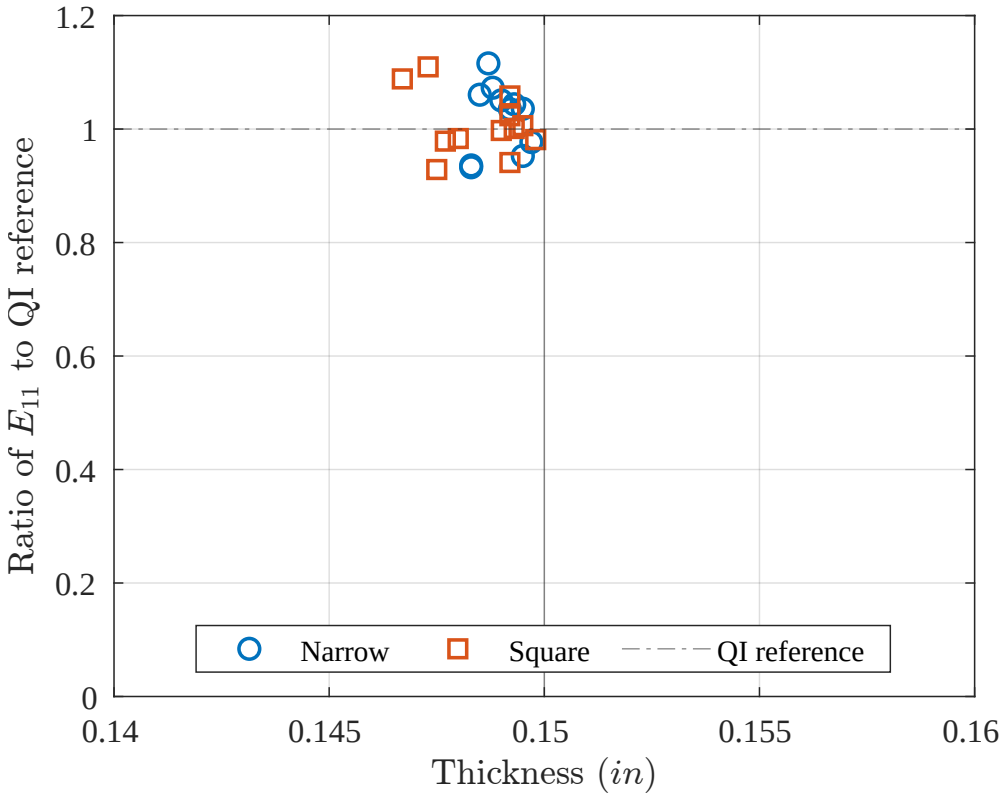

Figure A.4: High-Flow, Narrow vs Square Platelet:
Scatterplot of E_{11} for nominally 0.15" thick specimens manufactured with narrow or square platelets, using a high-flow process

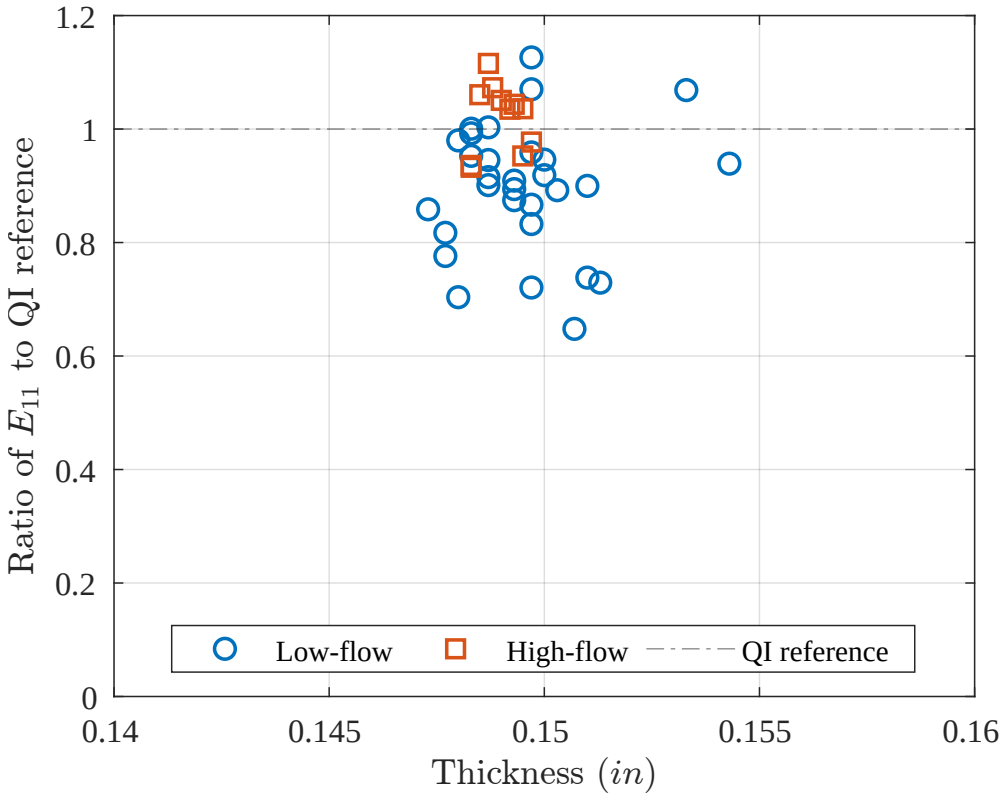

Figure A.5: Narrow Platelet, High-Flow vs Low-Flow:
Scatterplot of E_{11} for nominally 0.25" thick specimens manufactured with narrow platelets, using either a low-flow process or a high-flow process

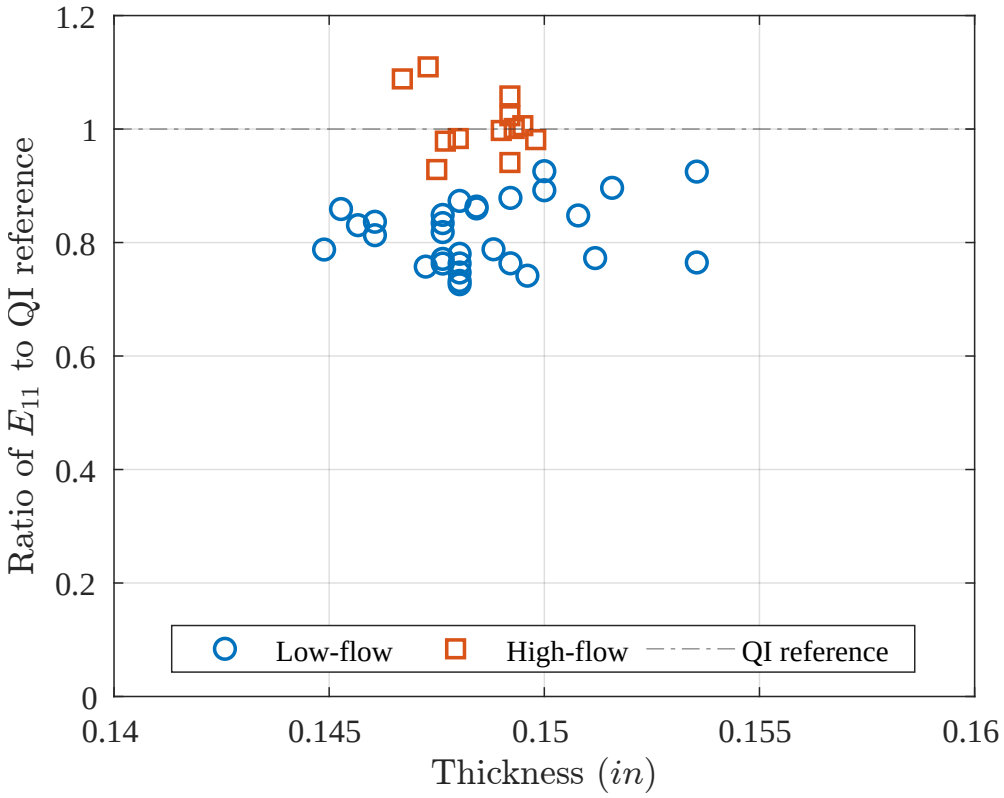

Figure A.6: Square Platelet, High-Flow vs Low-Flow:
Scatterplot of E_{11} for nominally 0.15" thick specimens manufactured with square platelets, using either a low-flow process or a high-flow process

Appendix B

IN-PLANE AND OUT-OF-PLANE FIBER ORIENTATION DISTRIBUTIONS

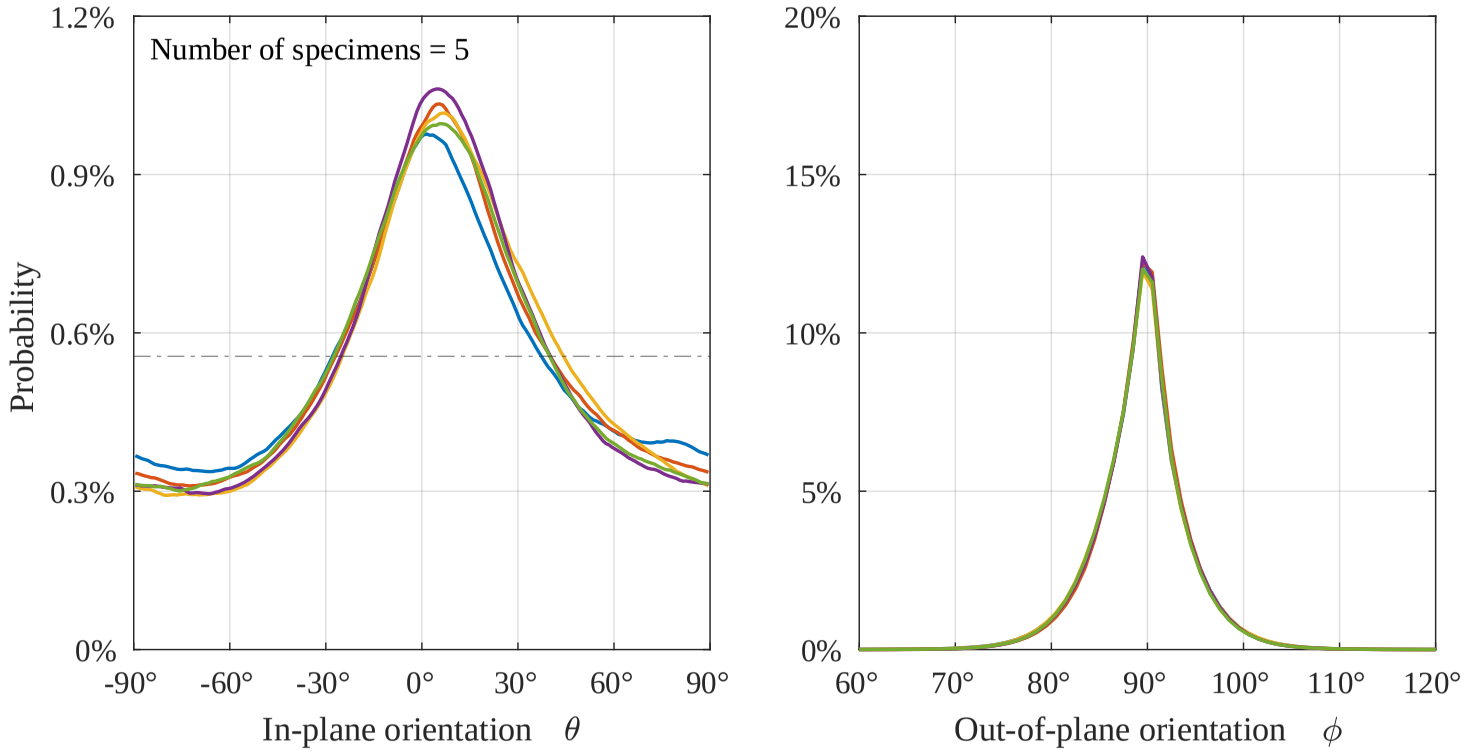

Figure B.1: Narrow Platelet, High-Flow: Probability distributions of in-plane and out-of-plane angles θ and ϕ

$\theta = 0°$ is aligned with the loading direction, $\phi = 90°$ is in-plane

Horizontal line represents an uniform in-plane distribution

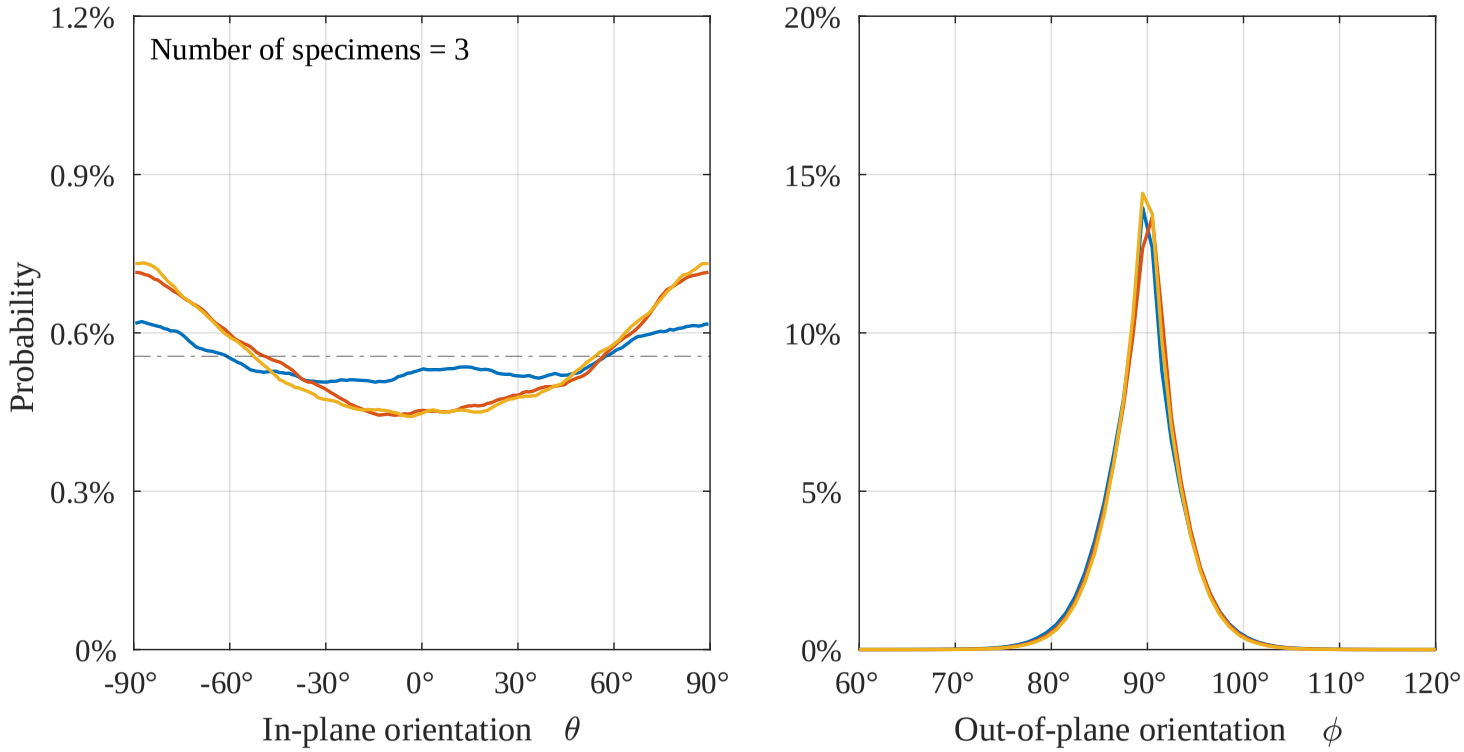

Figure B.2: Narrow Platelet, Low-Flow: Probability distributions of in-plane and out-of-plane angles θ and ϕ

$\theta = 0°$ is aligned with the loading direction, $\phi = 90°$ is in-plane

Horizontal line represents an uniform in-plane distribution

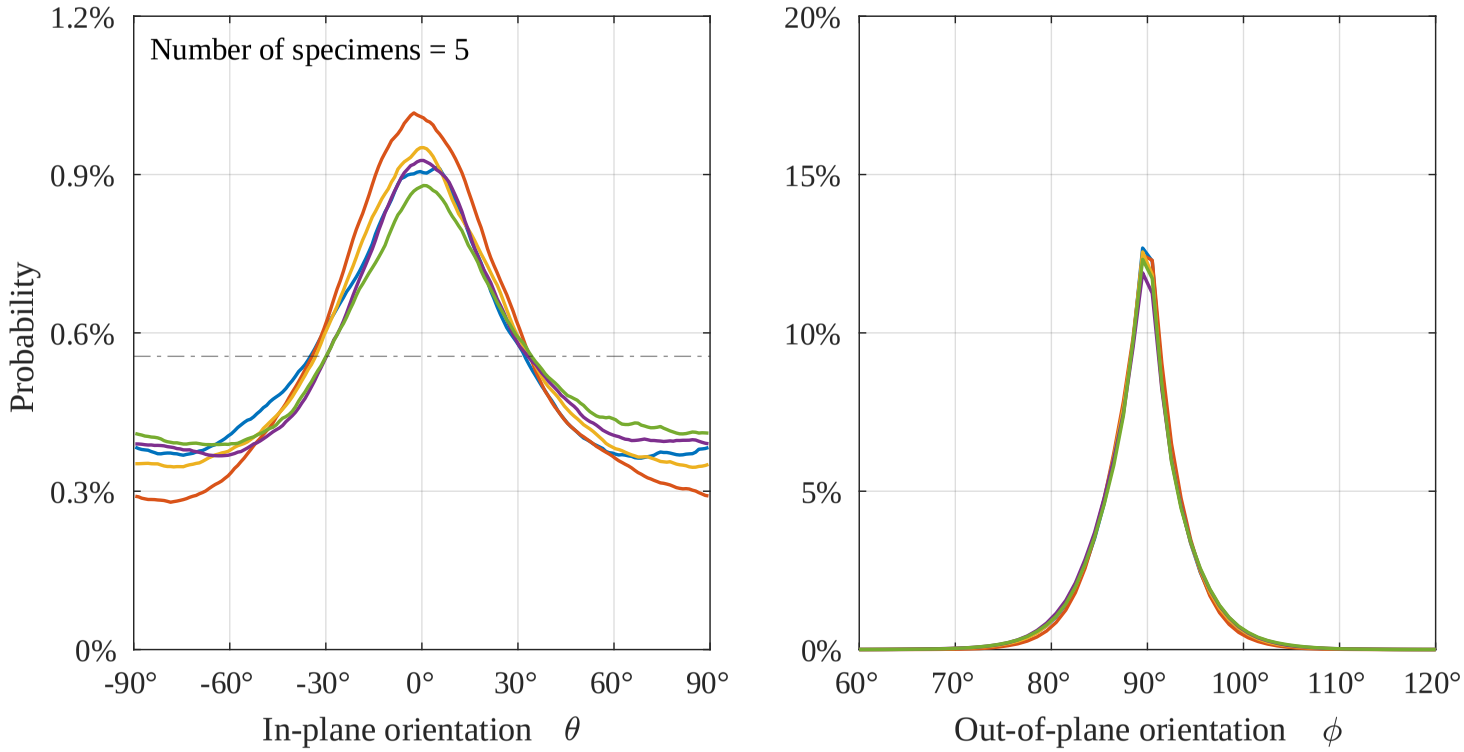

Figure B.3: Square Platelet, High-Flow: Probability distributions of in-plane and out-of-plane angles θ and ϕ

$\theta = 0°$ is aligned with the loading direction, $\phi = 90°$ is in-plane

Horizontal line represents an uniform in-plane distribution

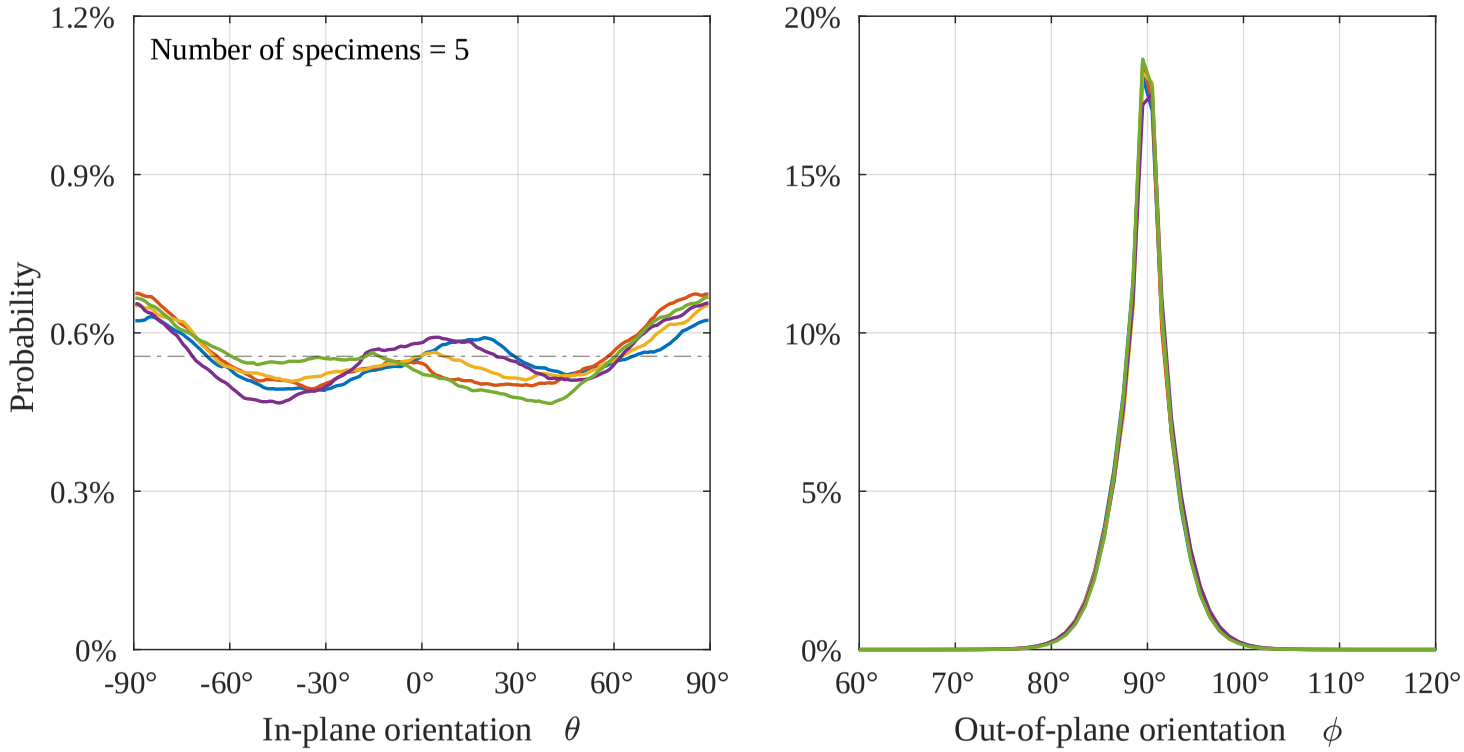

Figure B.4: Square Platelet, Low-Flow: Probability distributions of in-plane and out-of-plane angles θ and ϕ

$\theta = 0°$ is aligned with the loading direction, $\phi = 90°$ is in-plane

Horizontal line represents an uniform in-plane distribution